Journal of Energy Storage 163 (2026) 121873

Contents lists available at ScienceDirect

Journal of Energy Storage

journal homepage: www.elsevier.com/locate/est

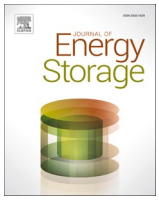

Research papers

Multi-layered thermal energy storage using phase change materials and molten salt for high-temperature waste heat recovery

Daniel Aviles [a,*], Emanuele Zanetti [a], Simone Mancin [b], Kamel Hooman [a]

[a] Department of Process and Energy, Delft University of Technology, Leeghwaterstraat 39, 2628 CB, Delft, the Netherlands
[b] Department of Management and Engineering, University of Padova, Stradella S. Nicola, 3, Vicenza, 36100, Italy

ARTICLE INFO

Keywords:
Thermal energy storage (TES)
Phase change material (PCM)
Molten salt
Hybrid TES
Waste heat recovery
Techno-economic analysis

ABSTRACT

Industrial high-temperature waste heat remains a largely underused high-grade energy source due to the limited techno-economic performance of conventional thermal energy storage (TES) systems. This paper proposes a novel multi-layered hybrid TES concept that combines phase change materials (PCMs) and molten salts to achieve high energy storage density while maintaining adequate heat transfer performance and stable charging-discharging behavior. The design incorporates two concentric layers filled with different melting temperature PCMs and a central core filled with molten salt, which serves as the heat transfer fluid and a high-temperature thermal buffer. The paper analyzes the thermal response, cycling behavior, and techno-economic performance of the hybrid TES for a given PCM pair. It benchmarks it against the two-tank TES across three scenarios: electricity generation with a power block, heat supply to an industrial process, and standalone energy storage. The optimized hybrid design reduces the levelized cost of electricity (LCOE), heat (LCOH), and storage (LCOS) by up to 2.6%, 12.4%, and 33.2%, respectively. The optimization also provides guidelines for the internal tube configuration, tube pitch, and energy storage allocation between the PCM layers. This article demonstrates the strong potential of our hybrid TES approach for cost-effective high-temperature energy storage.

1. Introduction

While worldwide efforts to decarbonize the energy and industrial sectors have intensified over recent decades, global warming remains a critical and persistent challenge. In line with the target to limit the global temperature rise to 1.5 °C [1], the European Commission aims to reduce greenhouse gas (GHG) emissions by at least 55% by 2030 [1] and reach climate neutrality by 2050 [2]. However, achieving these goals will require significant improvement in the industry sector, which is responsible for nearly half of the global CO2 emissions [3] and around 30% of global energy consumption [4]. Approximately 70% of the industrial energy demand is used for heat [5], most of which is still supplied by fossil fuels [6]. Some intensive heating processes require an unavoidable energy surplus [7], leading to considerable heat waste of up to 50% of the process energy [5], with about 30% lost through the flue gases [8].

The heat losses are more significant in high-temperature processes, such as those in the chemical, iron, and steel-making factories [9]. For instance, waste heat above 500 °C represents nearly 42% of Europe's total industrial waste heat [10]. Cost-effective valorization, recuperation, and reuse of high-temperature waste heat could reduce dependence on fossil fuels [11,12]. Nevertheless, several challenges remain regarding the intermittent nature of the industrial processes and the mismatch between the waste heat availability and the heat required by downstream applications [13]. Thermal energy storage (TES) provides an efficient solution to decouple the heat supply and demand, giving flexibility and consistency to the system [14]. However, preserving the exergy of high-grade waste heat streams requires high-temperature TES technologies.

One of the most common ways to store heat at high temperatures is by using molten salts. The two-tank molten salt configuration is a mature and well-studied approach for high-temperature TES [15]. In this configuration, molten salt is the heat transfer fluid (HTF) and the storage medium. The arrangement consists of two tanks connected to the heat-demanding application, typically a power block or an industrial process. The hot tank stores the HTF at high temperature after it has absorbed energy from the source. Once the thermal energy is transferred to the heat-demanding application, the cold tank maintains the HTF at a lower temperature until the next cycle [16,17]. Although this technology allows a straightforward operation, the associated capital costs remain a limitation for its adoption.

* Corresponding author.
E-mail address: D.E.AvilesCedeno@tudelft.nl (D. Aviles).

https://doi.org/10.1016/j.est.2026.121873
Received 14 October 2025; Received in revised form 15 March 2026; Accepted 27 March 2026
Available online 8 April 2026

Nomenclature

Symbols

C_p	specific heat [kJ/kg K]
C_{sys}	capital cost [USD]
$C_{O\&M,t}$	operating and maintenance cost in year t [USD]
d	discount rate [−]
E	energy stored [kJ]
E_t	net electricity generation in year t [MWh_e]
f_l	liquid fraction [−]
H	tank height [m]
h	convective heat transfer coefficient [W/m^2 K]
h_{sl}	melting enthalpy (latent heat of fusion) [kJ/kg]
k	thermal conductivity [W/m K]
m	mass [kg]
$\dot{m}$	mass flow rate [kg/s]
N	number of internal tubes connected to a header [−]
n	project lifetime [years]
Q_t	heat delivered in year t [MWh_{th}]
$Q_{dis,t}$	discharged thermal energy in year t [MWh_{th}]
$\dot{Q}$	heat transfer rate [W]
R_{pipe}	outer radius of the internal tubes [m]
r_0	inner radius of the internal tubes [m]
T	temperature [°C] or [K]
T_{m1}	solidus temperature [K]
T_{m2}	liquidus temperature [K]
t	time [s]
UA	thermal conductance [W/K]
v	velocity [m/s]

Greek symbols

ρ	density [kg/m^3]

Subscripts

dsch	discharging stage
el	element
fg	flue gases
in	inlet
ins	insulation
l	liquid phase
max	maximum
min	minimum
mt	melting
ms	molten salt
pipe	internal tubes
out	outlet
r	radial direction
s	solid phase
z	axial direction

Abbreviations

EAF	electric arc furnace
HRU	heat recovery unit
HTF	heat transfer fluid
HX	heat-demanding application heat exchanger
LCOE	levelized cost of electricity
LCOH	levelized cost of heat
LCOS	levelized cost of storage
PCM	phase change material
TES	thermal energy storage
TIT	temperature indicator transmitter sensor

In recent decades, phase change materials (PCMs) have attracted attention for their potential in multiple energy storage applications, including waste heat recovery, building energy management, and power generation [18]. PCMs store significant energy during phase transitions as latent heat. The capacity to absorb and release heat at a nearly constant temperature makes PCMs ideal for integration with thermal processes, minimizing thermal cycling losses and improving system efficiency [19]. Several authors have categorized and listed PCM based on their properties for low, medium, and high temperature applications [20–22]. However, their industrial use is currently concentrated in low and medium-temperature systems.

Although PCMs offer significant advantages for TES, their low thermal conductivity is still a prominent problem affecting the charging and discharging cycles [23]. Two of the most studied PCM-based configurations to address this limitation are packed bed tanks with encapsulated PCMs and shell-and-tube heat exchangers filled with PCMs [24]. The encapsulation method implies enclosing the PCMs within a high thermal conductivity material, optimizing the effective surface area per volume of the storage medium [25]. Nevertheless, this method is not yet suitable for high-temperature applications. PCM-based shell-and-tube heat exchangers are a preferred alternative due to their simplicity, cost-effectiveness, and scalability [26]. Their design resembles traditional shell-and-tube heat exchangers, with HTF flowing within the tubes, while the PCM, occupies the shell.

Several researchers have investigated PCM-based heat exchangers for TES applications. Li et al. conducted experimental and analytical studies using this configuration to cool a data center. Their results highlight critical parameters affecting the TES performance, such as the specific surface area and the tube length-to-diameter ratio [27]. Fragnito et al. performed numerical and experimental investigations on a vertical PCM-based shell-and-tube heat exchanger for cooling. Their model found that only 39% of the PCM mass suffered a complete phase change process [28]. Bianco et al. further optimized their model's geometry using a genetic algorithm, successfully increasing the usage of the PCM mass up to 70% [29]. Huang et al. evaluated the benefits of incorporating a shell-and-tube PCM heat exchanger inside an existing cooling and heating plant. The results showed an operational time increase of 65% and a reduction of the switch-on cycles by 33.5% [30].

Among the shell-and-tube PCM-based TES, the cascaded configuration has exhibited outstanding results. This approach overcomes the limitation of single-PCM designs by using multiple PCMs in a cascaded configuration [26]. Arranging the PCMs according to their melting temperature maintains an almost constant temperature difference between the PCM and the HTF, thus keeping a uniform heat transfer rate [31,32]. Furthermore, it has been demonstrated that cascaded systems require shorter charging and discharging cycles, exhibit higher exergy efficiency, and recover about 10% more exergy over 24-h cycles than non-cascaded systems [33]. Tehrani et al. [26] and Prieto et al. [19] have proposed cascaded PCM shell-and-tube TES for CSP plants; however, they didn't achieve considerable improvement and concluded that further model studies are required.

The open literature indicates a research gap regarding the design of cost-effective TES for industrial waste heat recovery applications operating above 500 °C. Moreover, there is a lack of techno-economic analysis comparing molten salts and PCMs-based TES for heat recovery applications. This article presents a hybrid high-temperature TES concept that combines PCMs and molten salts to achieve a higher energy storage density as compared to molten salts-based systems, without compromising the energy output rate required by the heat-demanding applications. The concept features a multi-layered storage tank with a molten salt core enclosed by different PCM layers. This work comprises the selection of feasible high-temperature PCM candidate materials, the

development of a dynamic numerical model for the PCM tank, and a multi-variable techno-economic optimization for a given PCM pair. To assess the effectiveness of the proposed TES concept, the article presents a case study on high-grade heat recovery in an electric arc furnace (EAF), comparing the performance and key economic parameters between the hybrid TES and the two-tank molten salt TES.

2. Storage concept

2.1. Operational framework of the proposed TES

The proposed approach combines molten salt and high-temperature PCMs to improve the energy storage density of high-temperature TES while reducing the overall system costs. Although PCMs provide high energy storage density at a lower price, maintaining molten salt in the design enables operational flexibility, as it serves as a storage medium and HTF. As a result, the heat-demanding application can draw the readily available sensible heat from the molten salt while extracting energy from the surrounding PCMs.

The proposed hybrid TES design is depicted in Fig. 1. The TES system consists of a cylindrical tank with molten salt located in its core and enclosed by concentric PCM layers, each separated by insulation. This configuration maintains the molten salt above the crystallization temperature over extended periods without requiring additional external heating. Unlike molten salt-based TES systems, which store energy as sensible heat within the molten salt, the hybrid design stores most of the energy in the PCM layers as latent and sensible heat.

To ensure an efficient heat transfer rate between the PCM and the HTF, the molten salt flows through the PCM layers using a homogenously distributed tube arrangement similar to the shell-and-tube PCM configuration, as illustrated in Fig. 1. The design keeps higher temperatures near the tank's core by extracting the heat from the outer layers toward the center of the tank, thus decreasing the external energy losses. The PCMs exhibit higher melting temperatures while approaching the core to ensure the HTF reaches the desired temperature output during the discharging stage. At the same time, the lower melting temperature of the exterior PCM layer allows for charging the TES easily due to the higher temperature gradient between the inlet HTF and the PCM.

The following sections explain the TES charging and discharging processes and the integration with the heat recovery unit.

2.2. Charging process

As previously mentioned, the present paper evaluates the integration of the hybrid TES system in high-grade waste heat recovery from an EAF. Accordingly, the charging and discharging processes are customized to the heat source's operational conditions. Fig. 2 provides the schematic of the hybrid TES charging process.

During the charging, the molten salt absorbs thermal energy from the EAF's flue gases via a heat recovery unit (HRU) integrated into the exhaust system. This unit works as a heat exchanger, where the molten salt flows through the interior of the tubes while the flue gases pass over the tube exterior surface. After being heated by the flue gases (state point 3), the three-way valve directs the molten salt to the TES to charge the PCM layers. The molten salt transfers the thermal energy to the PCM layers as it flows through the internal tubes, starting from the interior and moving toward the exterior of the TES.

As the TES outlet temperature increases during the PCM charging, Pump 1 adjusts the mass flow in the loop to maximize thermal energy recovery from the flue gases. The pump operates under a standard PI feedback controller that uses the temperature signal from the temperature indicator transmitter (TIT) to regulate its rotational speed via a variable-frequency drive. Because the pump speed dynamics are orders of magnitude faster than the thermal dynamics of the TES, the control loop is assumed to operate in quasi-steady state. The HRU considers a bypass to release the flue gases when the pump reaches the maximum mass flow rate, or the TES is completely charged.

2.3. Discharging process

During the discharging, the molten salt flows through the HRU and the TES to supply energy to the heat-demanding application, as presented in Fig. 3. After transferring its energy (state point 8), the three-way valve splits the low-temperature molten salt stream into two paths. The first stream absorbs thermal energy from the flue gases via the HRU, like in the charging process. The second stream enters the TES to remove the energy previously stored in the PCM layers. To do so, the molten salt (state point 5) flows through the internal tubes, this time starting from the exterior and moving toward the interior of the TES.

Since the PCM layers have different melting temperatures, the HTF reaches the required outlet temperature by extracting the sensible and latent heat from each layer. The inner PCM layer, which has a higher melting temperature, enables achieving the target high outlet

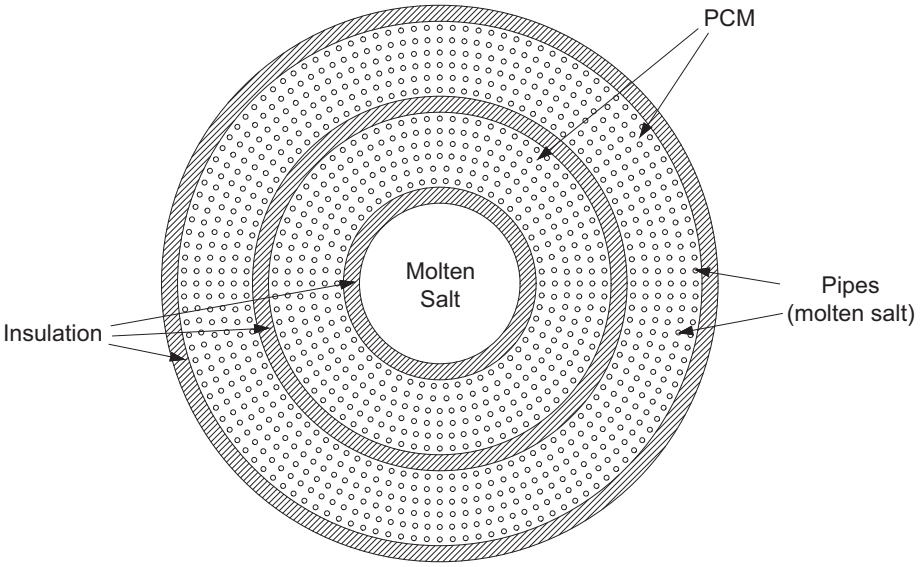

Fig. 1. Schematic cross-section of the hybrid TES.

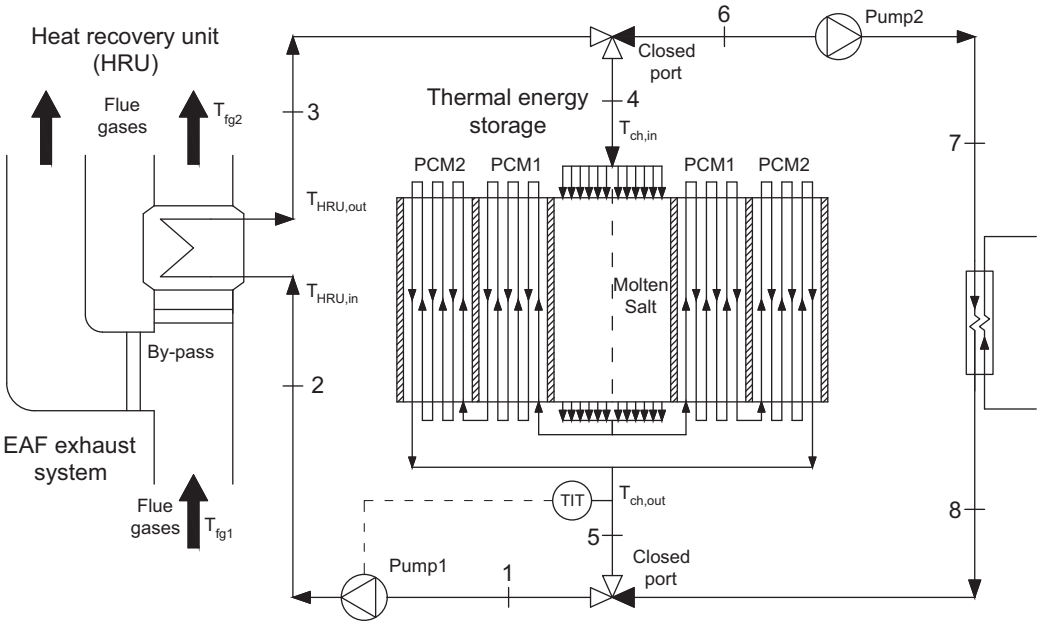

Fig. 2. Schematic of the waste heat recovery unit integrated with the hybrid TES during the charging process.

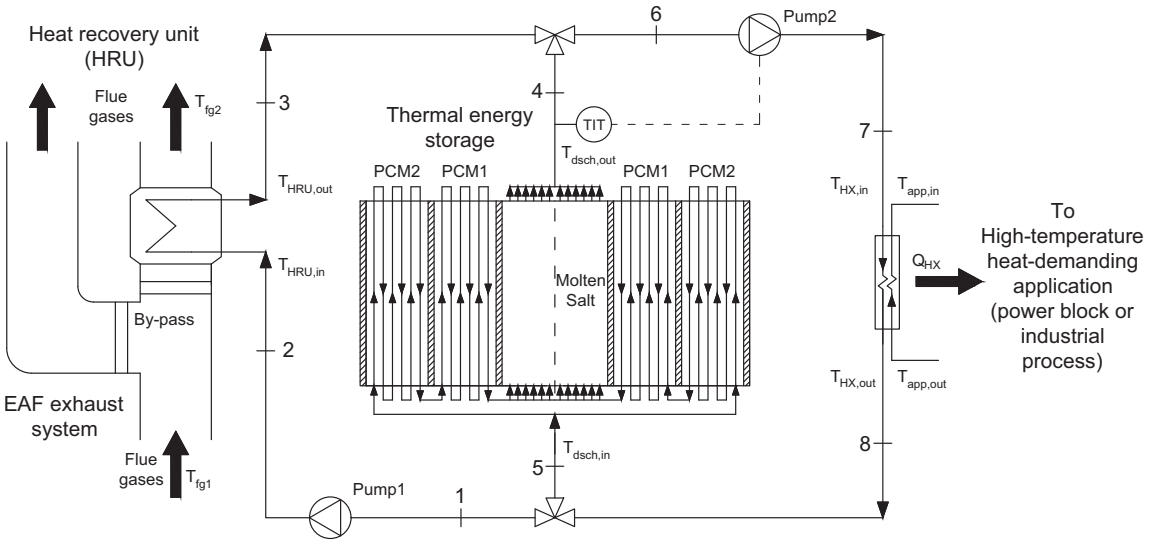

Fig. 3. Schematic of the waste heat recovery unit integrated with the hybrid TES during the discharging process.

temperatures. This configuration resembles a cascaded latent heat storage but enhances the performance by maximizing the use of the sensible heat.

As the molten salt absorbs the sensible heat above the melting temperature and then the latent heat, its outlet temperature gradually decreases over time (state point 4). Both streams, the first coming from the HRU and the second from the TES, recombine at the three-way valve. To compensate for the temperature fluctuations, Pump 2 adjusts the mass flow rate based on the TIT measurement, maintaining a constant heat flow rate to the heat-demanding application (such as an industrial process or power block). As in the charging process, the control loop is assumed to operate in a quasi-steady state due to the slow thermal dynamics of the TES.

2.4. Flow arrangements

The flow arrangement in the internal tubes of the TES is a critical variable for achieving an efficient heat transfer rate between the molten salt and the PCM during charging and discharging. The design must maximize the tube utilization, extracting and storing as much thermal energy as possible, while ensuring a feasible operation and construction. Natural convection in PCM-based TES can enhance heat transfer; however, it also leads to losses due to irreversibilities and thermal mixing, making it difficult to maintain the required high-temperature output over extended periods.

Fig. 4 illustrates three possible TES tube configurations. Fig. 4a and b show configuration 1, which consists of multiple rows of tubes that cross the PCM layers with alternating flow directions. A dedicated header at both the top and bottom of the tank connects the tubes in each row. This arrangement enhances the heat transfer rate by repeatedly circulating molten salt through the PCM layers. However, the design requires one header per row, resulting in considerable number of headers, increasing both the complexity and cost of the system. Additionally, the alternating flow creates vertical temperature gradients in the PCM, resulting in cold

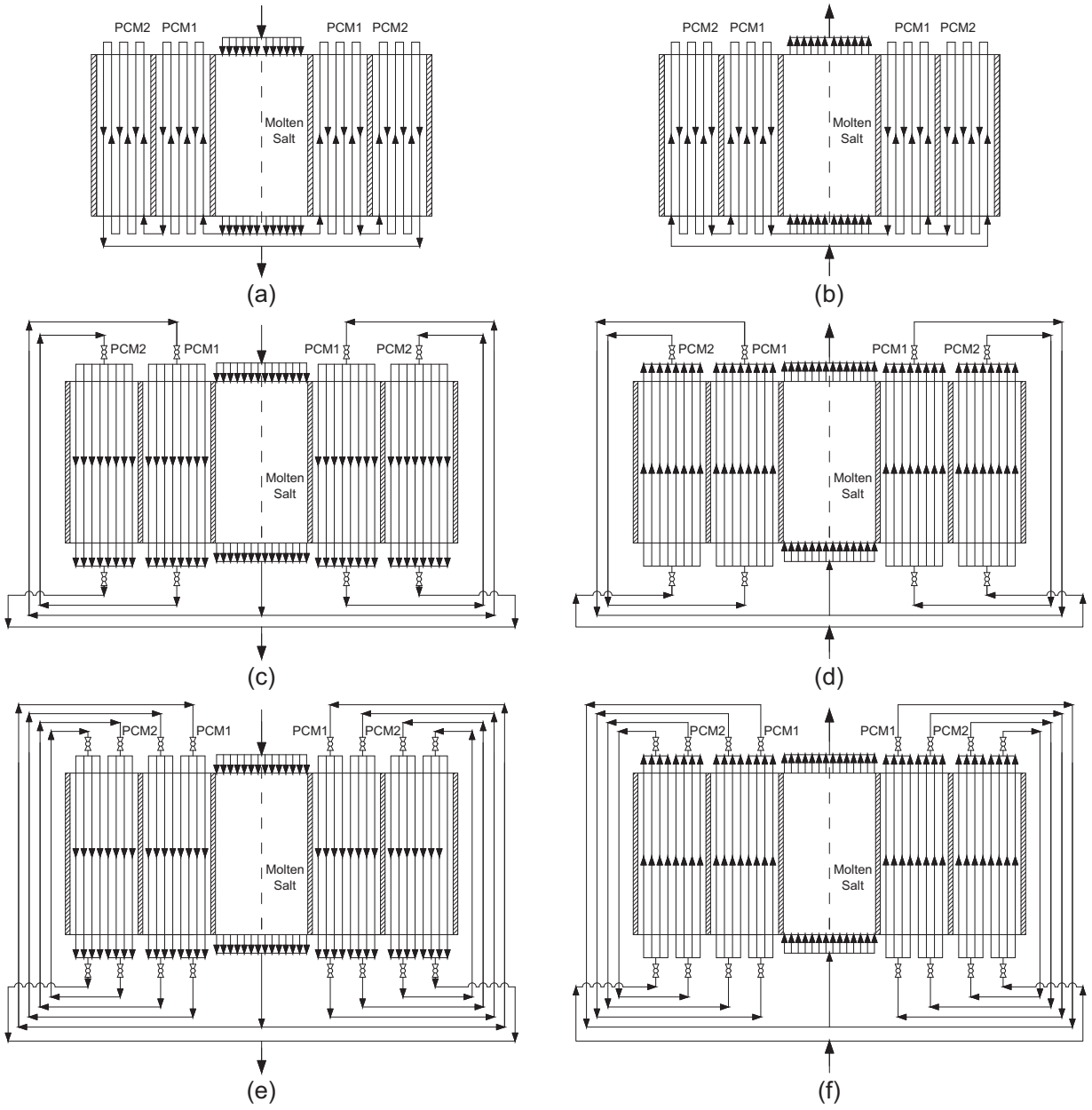

Fig. 4. Tube configurations in the TES during charging (left) and discharging (right) processes: (a–b) Configuration 1, (c–d) Configuration 2, (e–f) Configuration 3.

and hot zones. Hence, this configuration promotes natural convection in the PCM.

Fig. 4c and d present configuration 2. This design features multiple rows of tubes distributed across the PCM layers, all connected to a common header at both the bottom and top of the tank. During the charging process, the high-temperature molten salt flows downward through the internal tubes, transferring energy to the PCM from the top to the bottom. As a result, the PCM reaches a higher temperature near the top, promoting thermal stratification. In contrast, during discharging, the low-temperature molten salt flows upward, removing energy from the bottom to the top of the PCM. Hence, the PCM temperature is lower near the bottom, maintaining thermal stratification in the TES. While this configuration simplifies the design by requiring only one header per layer, it significantly limits the heat transfer rate as the molten salt circulates through the PCM layer only once.

Lastly, Fig. 4e and f illustrate configuration 3 where a common header connects multiple rows of tubes, resulting in many headers per PCM layer. The configuration adopts the same stratification strategy as the previous design, maintaining higher temperatures at the top of the tank by controlling the direction of the flow during both charging and discharging processes. This design achieves a trade-off between the previous two configurations, circulating the flow several times through the PCM layers, while requiring fewer headers for its operation.

In the present work, the TES is intentionally designed to promote thermal stratification in the PCM by controlling the molten salt flow direction within the internal tubes of the TES. Thermal stratification in shell-and-tube TES designs has been shown to limit the buoyancy-driven mixing in the PCM [28]. Furthermore, the high tube density within the PCM reduces the characteristic length scale for buoyancy-driven flow, allowing natural convection effects to be neglected with minimal error [34,35].

3. Modeling

This section presents the numerical model for the hybrid TES system and its integration for industrial waste heat recovery. The model

captures transient interactions during the charging and discharging processes, allowing for a holistic understanding of the variables at every point of the TES.

3.1. Assumptions

The system is modeled using a 2-D axisymmetric representation of the tank. The following key assumptions are made to get a trade-off between the accuracy of the results and the computational complexity and runtime:

- The PCMs are isotropic (each PCM has identical thermophysical properties in all directions).
- The thermophysical properties of the PCMs and the molten salt remain constant with the temperature (for both liquid and solid phase).
- The volume change during the melting or solidification processes is neglected.
- Axial conduction in the molten salt inside the tubes is negligible.
- Natural convection inside the PCM is neglected.
- The surrounding air temperature is spatially uniform at any given time.

3.2. Governing equations

The two-dimensional axisymmetric model comprehends specific energy equations for the PCM layer, the internal tubes, the molten salt core, and the insulation layers.

Firstly, the energy equation for the PCM can be written as shown in Eq. (1). This model is based on previous studies carried out by Tehrani et al. [26], Prieto et al. [19], and Liu et al. [36], which focuses on PCM modeling and cascaded shell-and-tube TES configurations. The equation has been adapted to match the design and operating conditions of the hybrid TES proposed in this study.

$$\rho_{PCM}C_{p,PCM}\frac{\partial T_{PCM}}{\partial t}+\rho_{PCM}h_{sl}\frac{\partial f_l}{\partial t}=\frac{\partial}{\partial z}\left(k_{PCM}\frac{\partial T_{PCM}}{\partial z}\right)+\frac{1}{r}\frac{\partial}{\partial r}\left(rk_{PCM}\frac{\partial T_{PCM}}{\partial r}\right) \tag{1}$$

where ρ, k_{PCM}, f_l, and h_{sl} represent the density, conductivity, liquid fraction, and melting enthalpy. The equation is based on the enthalpy method, which linearizes enthalpy in the mushy zone within a small temperature interval ΔT_{mt} defined between the solidus T_{m1} and the liquidus temperature T_{m2}. The liquid fraction, conductivity, and specific heat are evaluated using Eqs. (2)-(4).

$$f_l(T)=\begin{cases}0 & T_{PCM}<T_{m1}\ (Solid\ phase)\\ \dfrac{T_{PCM}-T_{m1}}{T_{m2}-T_{m1}} & T_{m1}\le T_{PCM}\le T_{m2}\ (Mushy\ zone)\\ 1 & T_{PCM}>T_{m2}\ (Liquid\ phase)\end{cases} \tag{2}$$

$$C_p(T)=\begin{cases}C_{ps} & T_{PCM}<T_{m1}\ (Solid\ phase)\\ \dfrac{C_{ps}+C_{pl}}{2} & T_{m1}\le T_{PCM}\le T_{m2}\ (Mushy\ zone)\\ C_{pl} & T_{PCM}>T_{m2}\ (Liquid\ phase)\end{cases} \tag{3}$$

$$k(T)=\begin{cases}k_s & T_{PCM}<T_{m1}\ (Solid\ phase)\\ k_l(f_l)+k_s(1-f_l) & T_{m1}\le T_{PCM}\le T_{m2}\ (Mushy\ zone)\\ k_l & T_{PCM}>T_{m2}\ (Liquid\ phase)\end{cases} \tag{4}$$

$$\Delta T_{mt}=\frac{T_{m2}-T_{m1}}{2} \tag{5}$$

The molten salt flowing through the internal tubes is modeled according to Eq. (6) [35].

$$\rho_{ms}C_{p,ms}\pi r_0^2\frac{\partial T_{ms}}{\partial t}+\frac{\dot{m}_{TES}C_{p,ms}}{N_{pipes}}\frac{\partial T_{ms}}{\partial z}=h_{overall}\left(T_{r=r_0}-T_{ms}\right)2\pi r_0 \tag{6}$$

In the equation, r_0, $\dot{m}_{TES}$, and N_{pipes} are the inner radius of the tubes, the mass flow rate through the TES, and the number of tubes connected to the dedicated header, respectively. The convective heat transfer coefficient of the molten salt inside the tubes, h_{pipe}, is calculated using the Gnielinski correlation [37].

The model considers the effects of the tube wall thickness on the overall heat transfer coefficient, $h_{overall}$, as described in Eq. (7) [38]. The tubes are made of stainless steel 316, having an average conductivity of 20 $Wm^{-1}\ K^{-1}$ in the TES operating temperature range [39].

$$h_{overall}=\frac{k_{pipe}h_{pipe}}{k_{pipe}+h_{pipe}r_0 ln\left(\frac{R_{pipe}}{r_0}\right)} \tag{7}$$

Eq. (8) models the molten salt inside the core layer of the TES. The effect of natural convection was not considered due to the molten salt's thermal stratification.

$$\rho_{ms}C_{p,ms}\frac{\partial T_{ms}}{\partial t}+\rho_{ms}v_{ms}C_{p,ms}\frac{\partial T_{ms}}{\partial z}=\frac{\partial}{\partial z}\left(k_{ms}\frac{\partial T_{ms}}{\partial z}\right)+\frac{1}{r}\frac{\partial}{\partial r}\left(rk_{ms}\frac{\partial T_{ms}}{\partial r}\right) \tag{8}$$

Finally, Eq. (9) presents the mathematical model for the insultation layers located between the PCM and the exterior of the tank.

$$\rho_{ins}C_{p,ins}\frac{\partial T_{ins}}{\partial t}=\frac{\partial}{\partial z}\left(k_{ins}\frac{\partial T_{ins}}{\partial z}\right)+\frac{1}{r}\frac{\partial}{\partial r}\left(rk_{ins}\frac{\partial T_{ins}}{\partial r}\right) \tag{9}$$

Eqs. (10)–(16) define the TES's internal and external boundary conditions. Specifically, Eqs. (10)–(11) describe the continuity of temperature and heat flux at the interfaces between each concentric layer (molten salt core, PCMs, and insulation). Eq. (12) represents the convective heat transfer at the external insulation surface exposed to the ambient air. The top and bottom surfaces of the tank are assumed adiabatic, as presented in Eq. (13). Finally, Eq. (14) describes the heat flux in the interface between the internal tubes and the surrounding PCM.

$$k_i\frac{\partial T_i}{\partial r}(r=R_i,z,t)=k_{i+1}\frac{\partial T_{i+1}}{\partial r}(r=R_i,z,t) \tag{10}$$

$$T_i(r=R_i,z,t)=T_{i+1}(r=R_i,z,t) \tag{11}$$

$$k_{ins}\frac{\partial T_{ins}}{\partial r}(r=R_{ext},z,t)=h_{air}(T(r=R_{ext},z,t)-T_{amb}(t)) \tag{12}$$

$$\frac{\partial T}{\partial z}(r,z=0,t)=0,\quad \frac{\partial T}{\partial z}(r,z=H,t)=0 \tag{13}$$

$$k_{PCM}\frac{\partial T_{PCM}}{\partial r}(r=R_{pipe},z,t)=h_{overall}\left(T(r=R_{pipe},z,t)-T_{ms}(z,t)\right) \tag{14}$$

For the initial condition, the TES is assumed to be fully charged at the maximum temperature, as shown in Eq. (15).

$$T(r,z,0)=T_{max} \tag{15}$$

3.3. Dynamic modeling of the TES and the HRU

The TES dynamic model was developed in MATLAB environment [40] using a finite volume discretization in both radial and axial directions. A Crank–Nicolson scheme is applied to the PCM and insulation layers to improve the stability and accuracy under transient conduction conditions. The molten salt flowing inside the tubes and the TES core are modeled using a fully implicit scheme to capture the advection-dominated energy transport. The TES and the HRU are dynamically integrated to evaluate the transient performance of the system.

3.3.1. Charging process

During the charging process (Fig. 2), the three-way valves connect the HRU and the TES in a closed loop, enabling the TES to charge using energy recovered from the flue gases. Eq. (16) determines the heat transfer rate from the flue gases, while Eq. (17) calculates the mass flow of molten salt entering the HRU.

$$\dot{Q}_{fg} = C_{p,fg}\dot{m}_{fg}\left(T_{fg1} - T_{fg2}\right) \tag{16}$$

$$\dot{m}_{ms,HRU} = \frac{\dot{Q}_{fg}}{C_{p,ms}\left(T_{HRU,out} - T_{HRU,in}\right)} \tag{17}$$

The HRU is modeled as a counterflow heat exchanger using the effectiveness-NTU method. Pump 1 regulates the molten salt mass flow rate to compensate for the TES outlet temperature increase. Eq. (18) corrects the conductance based on the mass flow rate variation [41].

$$UA = UA_{ref}\left(\frac{\dot{m}_1}{\dot{m}_{1,ref}}\right)^{0.8}\left(\frac{\dot{m}_2}{\dot{m}_{2,ref}}\right)^{0.8}\left(\frac{\dot{m}_{1,ref}^{0.8} + \dot{m}_{2,ref}^{0.8}}{\dot{m}_1^{0.8} + \dot{m}_2^{0.8}}\right) \tag{18}$$

Fig. 5 shows the flowchart of the TES charging process. The model considers HRU–TES coupling, molten salt mass flow rate regulation, and the phase-change behavior of the PCM layers. It captures the transient changes in the TES temperature field and the outlet molten salt temperature by solving these steps at each time interval.

3.3.2. Discharging process

During the discharging process, the three-way valves connect the HRU, TES, and the heat-demanding application heat exchanger (HX), as shown in Fig. 3. The HX outlet temperature is equal to the inlet temperatures of both the TES and the HRU. In this phase, the HRU operates close to its design conditions, regulating the molten salt mass flow rate to compensate for the small deviations in the HX outlet temperature. Eq. (19) shows the energy balance to calculate the TES energy demand, while Eq.(20) gives the TES mass flow rate using the previous time step temperatures.

$$\dot{Q}_{TES} = \dot{Q}_{HX} - \dot{Q}_{HRU} \tag{19}$$

$$\dot{m}_{TES} = \frac{\dot{Q}_{TES}}{C_{p,ms}\left(T_{dsch,out} - T_{dsch,in}\right)} \tag{20}$$

Eq. (21) calculates the HX inlet temperature, accounting for the mixing of TES and HRU outlet stream at the three-way valve.

$$T_{HX,in} = \frac{\dot{m}_{TES}\left(T_{dsch,out}\right) + \dot{m}_{ms,HRU}\left(T_{HRU,out}\right)}{\dot{m}_{TES} + \dot{m}_{ms,HRU}} \tag{21}$$

Fig. 6 shows the flowchart of the TES discharging process. The model accounts for HRU–TES–HX coupling, the molten salt mass flow rate regulation, and the PCM phase-change behavior. It assumes a constant thermal output power and a fixed HX outlet temperature for the industrial case, as the end-use conditions depend on the specific application. In contrast, when coupled with a power block, the model calculates the HX outlet temperature from the dynamic thermodynamic interaction with the Rankine cycle.

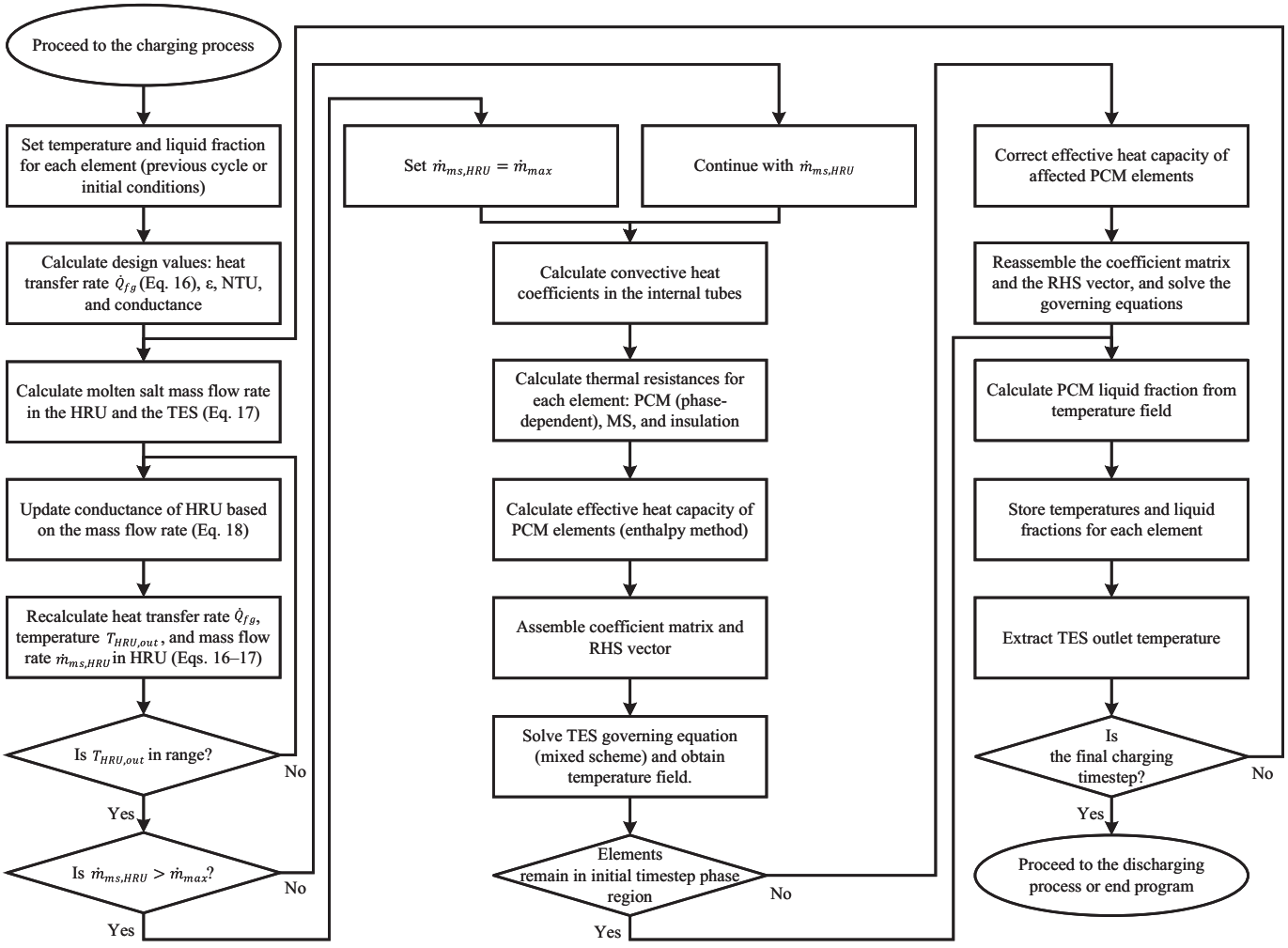

Fig. 5. Flowchart of the TES charging process.

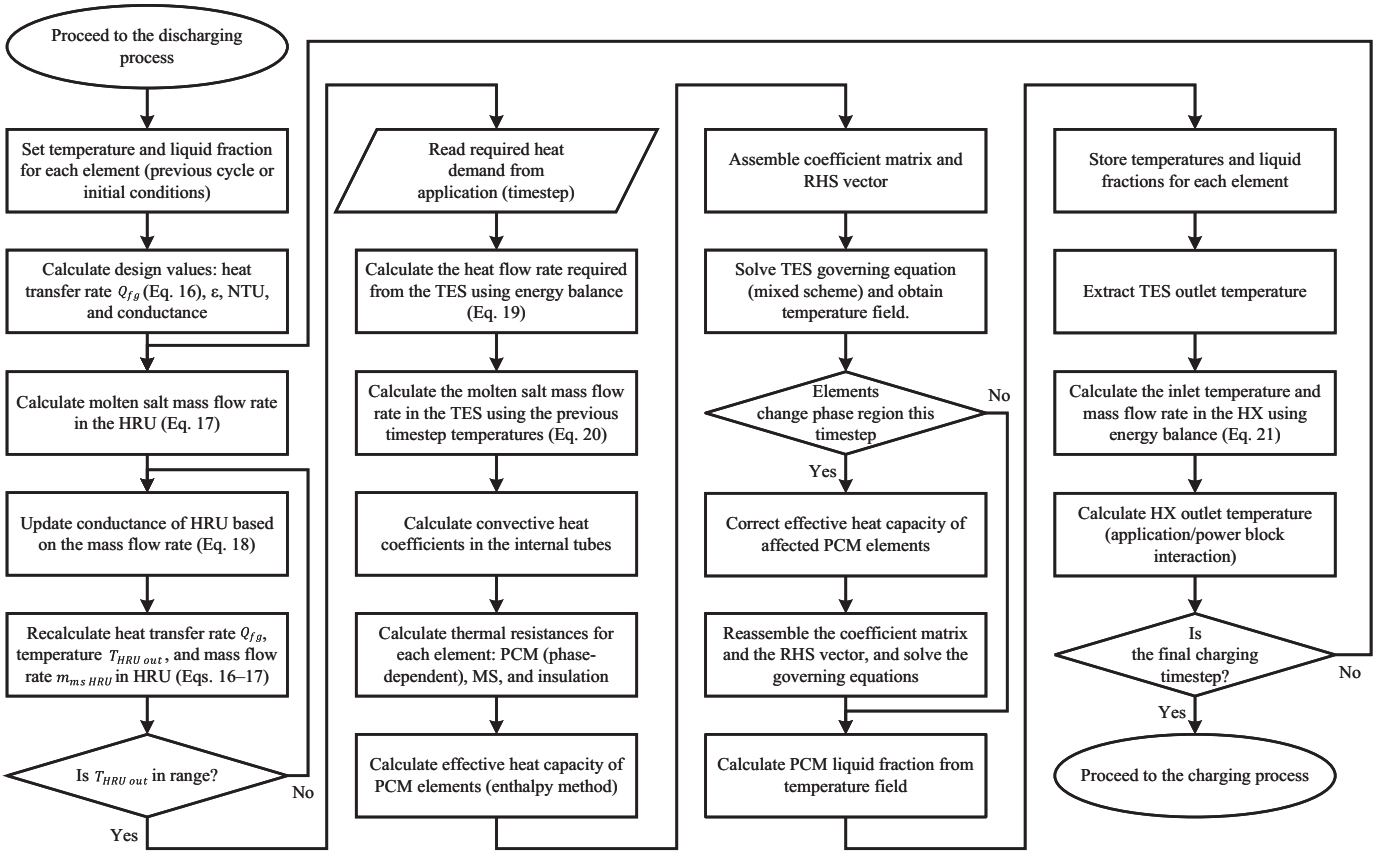

Fig. 6. Flowchart of the TES discharging process.

3.4. Model validation

Fig. 7 compares the predicted TES outlet temperature from the present numerical model with experimental data reported by Fragnito et al. [28] for a PCM-based shell-and-tube heat exchanger. The model was adapted to match the reported PCM thermophysical properties, geometric configuration, inlet conditions, and environmental parameters of the experimental system. This comparison assesses the validity of the governing equations and modeling assumptions. Although the operating temperature range and materials differ from those in the current application, the heat transfer mechanisms and phase-change behavior are equivalent. The comparison results in a root mean square

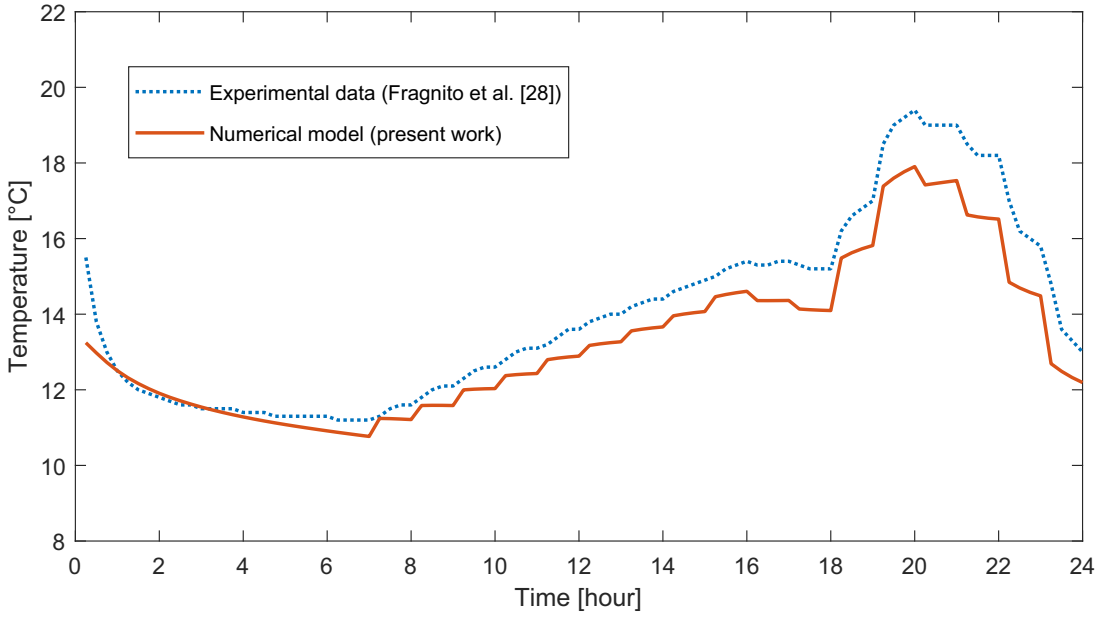

Fig. 7. Comparison between numerical model prediction and experimental temperature measurements reported by Fragnito et al. [28] for a PCM shell-and-tube configuration.

error of 0.9 K, providing confidence in the current modeling approach.

3.5. Dynamic evaluation of stored energy in the TES

The energy stored in the proposed TES is critical for evaluating its effectiveness during charging and discharging cycles. Eq. (22) determines the maximum usable energy that can be stored in the PCM layers, as sensible heat in the solid and liquid phases and as latent heat during phase change. Here, T_{max} and T_{min} denotes the maximum and minimum allowable temperatures in the TES.

$$E_{max} = \sum_{i=1}^{nP} \left(m_i C_{pl} (T_{max} - T_{mt\,i}) + m_i h_{sl\,i} + m_i C_{ps} (T_{mt\,i} - T_{min}) \right)_{PCM} \quad (22)$$

The energy stored in the TES at every time step is calculated by summing the stored energy in each element (E_{el}) across all layers (nP), radial divisions (nr), and axial divisions (nz), as shown in Eqs. (23) and (24).

$$E_{TES}(t) = \sum_{i=1}^{nP} \sum_{j=1}^{nr} \sum_{k=1}^{nz} E_{el\,i,j,k}(t) \quad (23)$$

$$E_{el}(T) = \begin{cases} m_{el} C_{ps} (T_{el} - T_{min}) & T_{el} < T_{m1} \\ m_{el} C_{ps} (T_{mt} - T_{min}) + f_l m_{el} h_{sl} & T_{m1} \le T_{el} \le T_{m2} \\ m_{el} C_{ps} (T_{mt} - T_{min}) + m_{el} h_{sl} + m_{el} C_{pl} (T_{el} - T_{mt}) & T_{el} > T_{m2} \end{cases} \quad (24)$$

The percentage of energy stored in the TES during the charge and discharge cycles, relative to its maximum usable capacity, is calculated using Eq. (25).

$$\%E(t) = \frac{E_{TES}(t)}{E_{max}} \quad (25)$$

The energy removed by the molten salt flow from the TES during each time step is calculated using the inlet and outlet TES temperatures, the mass flow and the time step, as shown in Eq. (26). The cumulative energy removed up to a given time is obtained using the Eq. (27).

$$E_{rem}(t) = \dot{m}_{TES} C_{p,ms} \left(T_{dsch,out} - T_{dsch,in} \right) \Delta t \quad (26)$$

$$E_{cum}(t) = \sum_{s=1}^{N} E_{rem}(s) \quad (27)$$

3.6. Candidate materials for the TES

Table 1 lists feasible high-temperature PCM and molten salt candidates for the TES and their thermophysical properties compiled from the literature. The PCMs' costs were estimated in this work based on their mass fraction composition. The prices of pure substances are provided in Appendix A.

3.7. Economic indicators

This work uses the levelized cost of electricity (LCOE), heat (LCOH), and storage (LCOS) as the main indicators to assess the feasibility of the proposed TES concept. These metrics are calculated as follows [45]:

$$LCOE = \frac{C_{sys} + \sum_{t=1}^{n} \frac{C_{O\&M,t}}{(1+d)^t}}{\sum_{t=1}^{n} \frac{E_t}{(1+d)^t}} \quad (28)$$

$$LCOH = \frac{C_{sys} + \sum_{t=1}^{n} \frac{C_{O\&M,t}}{(1+d)^t}}{\sum_{t=1}^{n} \frac{Q_t}{(1+d)^t}} \quad (29)$$

$$LCOS = \frac{C_{sys} + \sum_{t=1}^{n} \frac{C_{O\&M,t}}{(1+d)^t}}{\sum_{t=1}^{n} \frac{Q_{dis,t}}{(1+d)^t}} \quad (30)$$

where C_{sys} denotes the total capital cost of the system, and $C_{O\&M,t}$ represents annual operating and maintenance costs in the year t. E_t is the net electricity generation, Q_t is the useful heat delivered, and $Q_{dis,t}$ is the discharged thermal energy from the TES, all in year t. The discount rate is d, and the project lifetime is n years. The project life is 25 years with a discount rate of 6.4% [46].

The capital and O&M costs for each sub-system were estimated from literature data, simulation outputs, and scaling factors, as summarized in Table 2. The capital cost for the hybrid PCM-molten salt TES was determined by summing the cost of its main elements. The storage material costs (PCM and molten salt) were calculated from unit prices in Table 1 and the mass per layer from the MATLAB simulation. Correlations developed by the National Renewable Energy Laboratory (NREL) for molten salt-based TES [44] were adapted by volume to estimate tank structure, instrumentation, foundation, electrical system, sitework, and insulation. Internal piping costs were determined from the number of tubes obtained by the simulation and their mass per unit length, including an 80% allowance for installation, fittings, valves, and headers. Stainless steel 316 ($4.4/kg) was assumed for the tank and piping to ensure corrosion resistance when operating with high-temperature PCM [47]. The detailed cost breakdown is presented in the results section.

Table 1
Thermophysical properties and estimated costs of candidate materials for the TES.

Material composition wt%	T_{mt} °C	k W/m·K	ρ_l kg/m^3	h_{sl} kJ/kg	C_{ps} kJ/kg·K	C_{pl} kJ/kg·K	Price* $/kg	Ref**
$MgCl_2$(60)–KCl(20.4)–NaCl(19.6)	380	0.744	1700	400	0.96	1.04	0.269	[42]
Li_2CO_3(32.1)–K_2CO_3(34.5)–Na_2CO_3(33.4)	397	2.02	2300	276	1.67	1.63	4.198	[20]
$MgCl_2$(39)–KCl(61)	435	0.81	2110	351	0.80	0.96	0.350	[20]
NaCl(48)–$MgCl_2$(52)	450	0.95	2230	430	0.92	1.00	0.190	[43]
NaCl(50)–$MgCl_2$(50)	450	0.96	2240	450	0.93	–	0.185	[20]
$MgCl_2$(64)–KCl(36)	470	0.83	2190	388	0.84	0.96	0.325	[20]
KCl(25)–$CaCl_2$(27)–$MgCl_2$(48)	487	0.83	2530	342	0.80	0.8	0.301	[20]
Na_2CO_3(55.6)–Li_2CO_3(44.4)	496	2.09	2320	370	1.80	2.09	6.606	[20]
Na_2CO_3(72)–Li_2CO_3(28)	498	1.85	2240	263	1.46	1.80	3.468	[20]
NaCl(33)–$CaCl_2$(67)	500	1.02	2160	281	0.84	1.00	0.189	[20]
$CaCl_2$(66)–KCl(5)–NaCl(29)	504	1.00	2150	279	1.17	1.00	0.203	[20]
K_2CO_3(65)–Li_2CO_3(35)	505	1.89	2260	344	1.34	1.76	4.762	[20]
$BaCl_2$(53)–KCl(28)–NaCl(19)	542	0.86	3020	221	0.63	0.80	0.374	[20]
Na_2CO_3(60)–Li_2CO_3(20)–K_2CO_3(20)	550	1.83	2380	283	1.59	1.88	2.711	[20]
$BaCl_2$(47) –$CaCl_2$(29)–KCl(24)	551	0.95	2930	219	0.67	0.84	0.385	[20]
Solar salt: $NaNO_3$(60)–KNO_3(40)	–	0.53	1772	–	–	1.53	1.1	[44]

* PCM blend prices have been calculated by mass-fraction weighting of pure constituent substances. Pure constituent prices are listed in Appendix A.
** Reference for thermophysical properties.

Table 2
Cost estimation basis for each sub-system.

Component	Capital cost estimation	O&M cost	Additional information
Power block	Power cycle: $1040/kWe; Balance of plant: $290/kWe [44]	Fixed: $66/kW-yr; Variable: $3.5/MWh [44]	A penalty was applied to the capital cost due to the smaller capacity (Penalty factor: 1.3)
Heat exchanger (HX)	Estimated with Aspen EDR [48]	5% of the capital cost	HX was designed in Aspen EDR for the required specifications [48]
Heat recovery unit (HRU)	Estimated with Aspen EDR [48]	5% of the capital cost	A penalty was applied to the capital cost to account for the modified configuration, auxiliary equipment, and additional instrumentation (Penalty factor: 2)
Two-tank molten salt TES	$22/kWh$_{th}$ [44]	5% of the capital cost	A penalty was applied to the capital cost due to the smaller capacity (×1.3 cost penalty)
Hybrid PCM-molten salt TES	Estimated from material cost (Table 1 and MATLAB simulation), NREL molten salt tank correlation, and piping requirements.	5% of the capital cost	The costing methodology is detailed in Section 3.7
Contingency	7% of capital cost	–	It was applied to each sub-system.

Table 3
Operational parameters of the EAF.

Parameter	Value
EAF Power	50 MW
Waste heat fraction	25%
Flue gases specific heat	1.1 kJ/kg·K [12]
Flue gases outlet temperature	700 °C
EAF operating days	300 days/year
Ambient temperature	20 °C

4. Results and discussion

4.1. Case definition

The present case study considers the continuous operation of a 50 MW EAF with the parameters listed in Table 3. The HRU-TES arrangement must be capable of supplying heat for 8 h, either to a 16 MW industrial process or to a power block with a nominal electrical power output of 6.5 MW. Table 4 summarizes the HRU-TES system requirements.

The techno-economic analysis assesses the system's feasibility using two TES configurations: a traditional two-tank molten salt TES and a hybrid PCM-molten salt TES. We analyzed each TES configuration in three applications: electricity generation, where the HRU-TES provides thermal energy to a power block; industrial heat supply, where the HRU-TES system delivers a constant heat rate to a high-temperature application (above 500 °C); and thermal energy storage, where the TES operates without a specific end-use. Table 5 summarizes the six modeled cases, including the economic indicator used to assess their performance.

Table 4
HRU-TES system requirements.

Requirement	Value
Thermal power output	16 MW$_{th}$
Electrical power output (nominal)	6.5 MW$_{e}$
Charging time	16 h
Discharging time	8 h
Maximum outlet temperature (molten salt stream)	550 °C
Minimum outlet temperature (molten salt stream)	500 °C
Minimum allowable TES temperature	280 °C

4.2. Baseline simulation

Although Table 1 presents different high-temperature PCMs to cover a wide range of operating temperatures, this study focuses on a fixed combination of materials that satisfies the required temperatures (Table 4) while maintaining a low storage material cost. Accordingly, we selected CaCl2(66)–KCl(5)–NaCl(29) for the internal PCM layer and MgCl2(60)–KCl(20.4)–NaCl(19.6) for the external PCM layer.

As described in Section 2.4, we evaluated different flow configurations in the hybrid TES (Fig. 4). Configuration 1 achieved the required outlet temperature but induced significant natural convection and required one header per row. Configuration 2 promoted thermal stratification and simplified the design to only two headers per layer but did not reach the target outlet temperature. Configuration 3 also promoted stratification while achieving the required outlet temperature with a feasible number of headers; therefore, we selected it for further simulations. Appendix B provides additional insight into the influence of the number of rows per header on the TES outlet temperature (Fig. B.1).

As defined in Section 4.1, we design the TES to compensate for the difference between the heat recovery from the HRU and the downstream energy demand. Our approach exploits the PCMs' storage capacity not only as latent heat but also as sensible heat within the operating temperature range. However, operating at the maximum usable energy of the TES (Eq. (22)) is impossible. The molten salt stream must maintain an outlet temperature above 500 °C during discharge, which requires a fraction of the PCM to remain at high temperature to sustain heat transfer to the molten salt stream. Therefore, in the baseline case, we operate the TES at 76% of its maximum usable energy, including the sensible and latent heat contributions.

We sized the molten salt core to supply at least 15 min of energy, serving as a thermal buffer during variations in mass flow rate. The PCM mass in each layer depends on the total TES energy capacity, the energy split between the PCM layers, the effective energy storage capacity of each PCM within the operating range, and the non-usable energy fraction required to maintain the temperature outlet above 500 °C. The TES sizing includes insulation between the molten salt core and the PCM

Table 5
Summary of the six analyzed cases.

Case	TES configuration	Application	Economic indicator	Sub-system
A I	Two-tank molten salt TES	Electricity generation	LCOE	TES + HRU + power block
A II	Hybrid PCM-molten salt TES	Electricity generation	LCOE	TES + HRU + power block
B I	Two-tank molten salt TES	Industrial heat supply	LCOH	TES + HRU + HX
B II	Hybrid PCM-molten salt TES	Industrial heat supply	LCOH	TES + HRU + HX
C I	Two-tank molten salt TES	Thermal energy storage only	LCOS	TES
C II	Hybrid PCM-molten salt TES	Thermal energy storage only	LCOS	TES

Table 6
Baseline design parameters of the hybrid TES system.

Parameter	Value
Energy storage capacity split	52% in PCM 1–48% in PCM 2
Molten salt core buffer capacity	15 min of energy supply
Concentric shell (3 layers) material	Stainless steel 316
Tube external diameter	25 mm
Tube wall thickness	1 mm
Tube material	Stainless steel 316
PCM layer 1 tube pitch	62.4 mm
PCM layer 2 tube pitch	61.1 mm
Internal insulation thickness	50 mm
External insulation thickness	200 mm
Rows per header	3

layers, as well as the external insulation. In the baseline case, we treat the tube pitches in each layer as decision variables based on the number of tubes per layer. Table 6 summarizes baseline design parameters for the hybrid TES system, and Table 7 gives an overview of the resulting TES geometry, materials, and configuration.

The power block (cases AI and AII) uses a conventional superheated Rankine cycle with reheat. At design-point conditions, we set the turbine inlet temperature and pressure to 470 °C and 120 bar, respectively, with a reheating temperature of 420 °C. Under these conditions, the cycle achieved an efficiency of 40.8%. In the hybrid TES case (AII), the TES outlet temperature decreases during discharging, which reduces the turbine inlet temperature. Hence, the cycle efficiency gradually declines from 40.8 to 39.7%, and the power output from 6.5 MW to 6.33 MW.

4.2.1. *Dynamic energy contributions and balance*

Fig. 8 illustrates the evolution of the sensible and latent energy contributions and the overall energy balance in the PCM layers of the TES during discharge. The molten salt flowing in the internal tubes extracts sensible heat from the liquid and solid phases, as well as latent heat during the solidification process, due to the local temperature gradient between the salt stream and the PCM. Hence, one region of a PCM layer may release sensible heat, while another region releases latent heat, depending on the local phase state, as further visualized in the following section. However, the molten salt cannot extract all the stored energy, since its outlet temperature must remain above 500 °C throughout the process. The unrecovered energy is mostly the sensible heat of the solid phase. Specifically, the proposed TES approach utilizes 88% of the latent heat, 41.9% of the sensible heat in the solid phase, and 100% of the sensible heat in the liquid phase of the PCMs. The figure also shows that the cumulative energy removed increases linearly, consistent with the constant heat flow rate required by the power block or the heat-demanding application. Finally, the energy balance, obtained by summing the stored energy and the cumulative energy removed, remains nearly constant, with environmental losses lower than 0.1%.

Table 7
Geometry and materials of the hybrid TES system.

Description	Material	Melting temperature [°C]	Height [m]	Radial Thickness [m]	Mass [kg]	Number of tubes
Molten salt core	$NaNO_3$(60)–KNO_3(40)	–	6	0.80	21,876	–
PCM layer 1	$CaCl_2$(66)–KCl(5)–NaCl(29)	504	6	2.12	288,079	6339
PCM layer 2	$MgCl_2$(60)–KCl(20.4)–NaCl(19.6)	380	6	1.16	234,287	6660

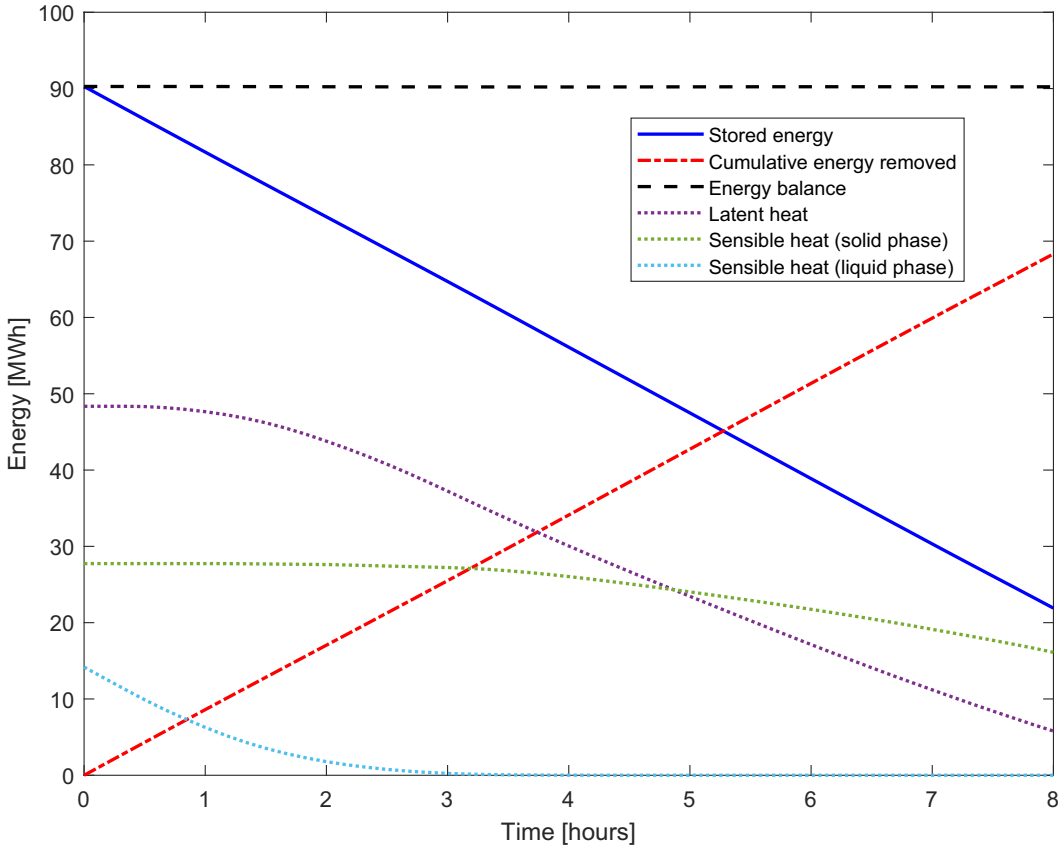

Fig. 8. Energy contributions and balance in the TES during discharge.

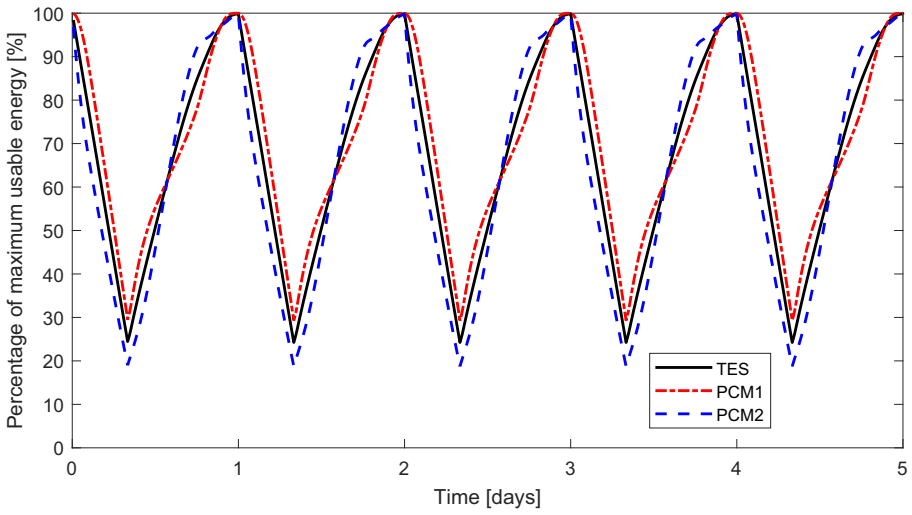

Fig. 9. Cycling behavior of the TES and each PCM layer.

4.2.2. Thermal cycling behavior

Fig. 9 illustrates the charge–discharge cycling behavior of the TES and each PCM layer (PCM1 and PCM2). Under baseline conditions, the TES charges up to 99.9% of its maximum usable capacity (Eq. (25)), corresponding to nearly full charging cycles. However, due to the residual thermal energy required to sustain the heat transfer to the molten salt stream, the TES only discharges up to 24.2%. PCM 2 charges and discharges more easily due to its lower melting temperature, utilizing up to 81.3% of its energy storage capacity. In contrast, PCM 1 charges and discharges more slowly because of its higher melting temperature, utilizing up to 69.7% of its storage capacity. These results highlight the importance of including both PCM layers; the second layer enables a higher and faster storage capacity, while the first layer enables reaching the required molten salt outlet temperatures.

Figs. 10–13 present the temporal and spatial evolution of the temperature and liquid fraction within the PCM layers. The results correspond to discharging at $t = 2$, 4, 6, and 8 h, and charging at $t = 12$, 16, 20, and 24 h. According to the temperature profiles of PCM1 (Fig. 10) and PCM2 (Fig. 12), PCM1 retains higher temperatures during discharge, especially near the molten salt core. This behavior enables the

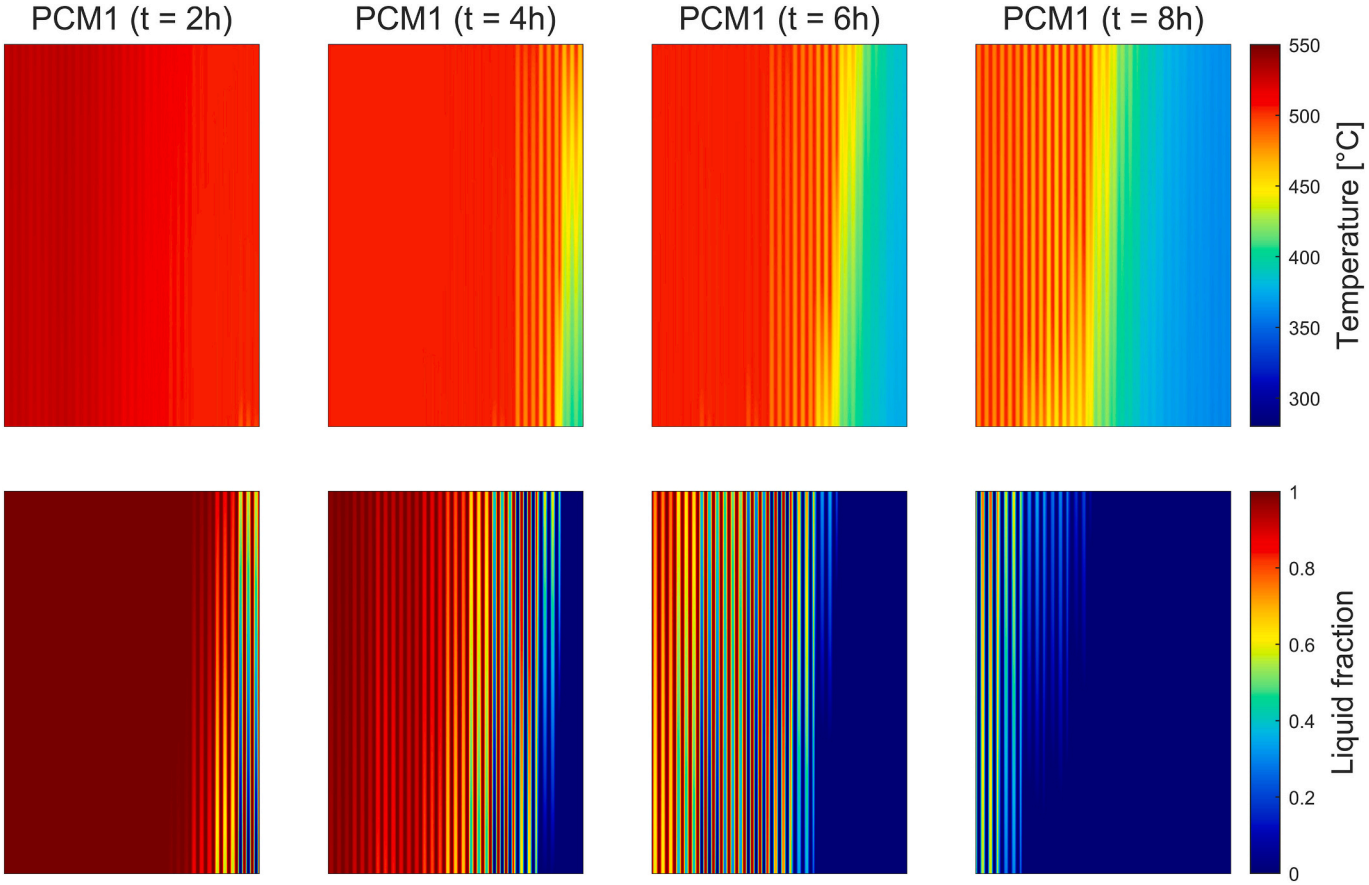

Fig. 10. PCM temperature (top) and liquid fraction (bottom) profiles for PCM layer 1 during discharging.

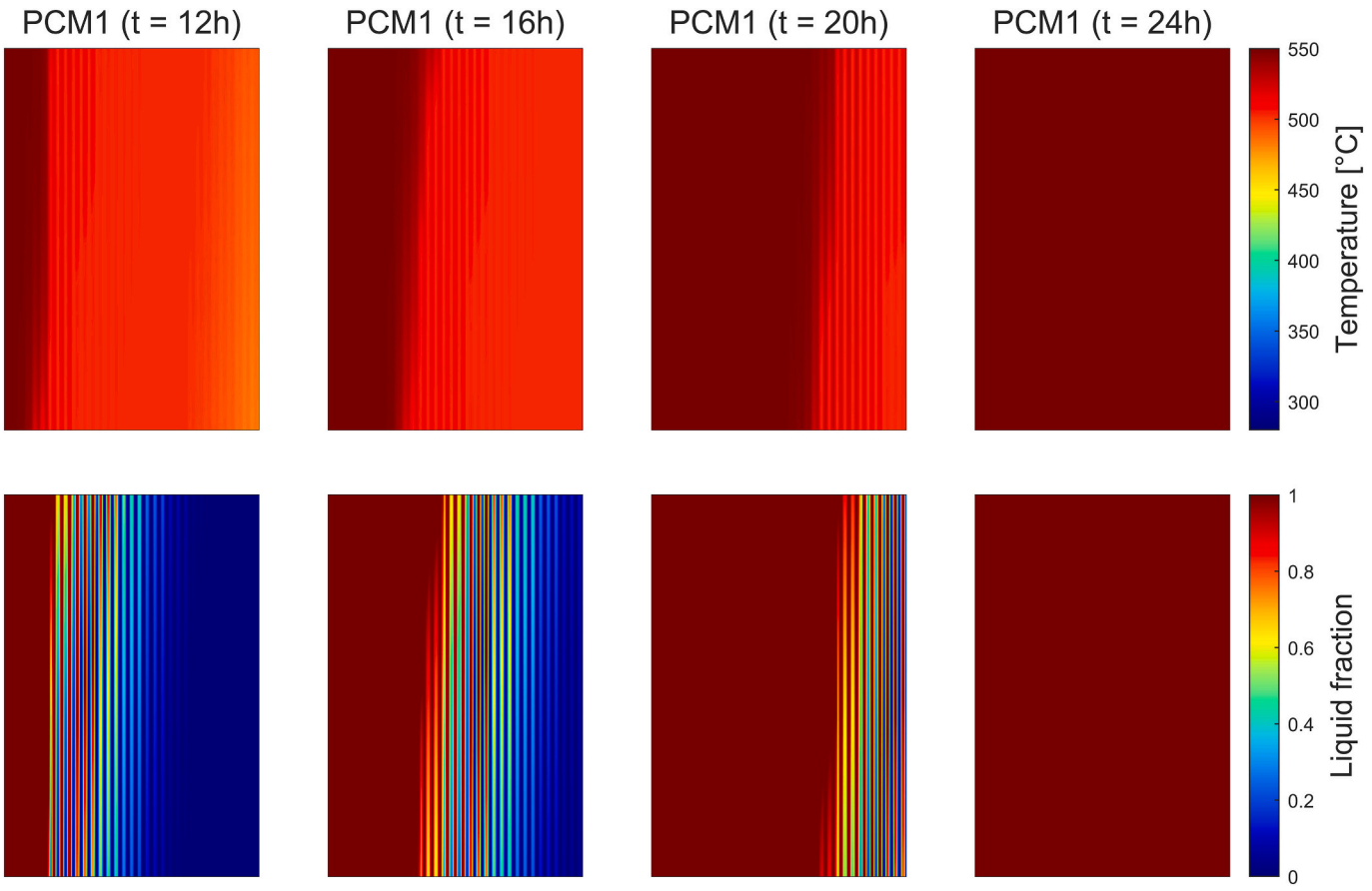

Fig. 11. PCM temperature (top) and liquid fraction (bottom) profiles for PCM layer 1 during charging.

TES to maintain the required molten salt outlet temperature.

Since PCM2 reaches lower temperatures during discharge, the TES utilizes a larger portion of its maximum storage capacity, as also shown in Fig. 9. Furthermore, the lower temperatures in the PCM2 region near the external wall reduce the temperature gradient with the surrounding environment, thereby decreasing ambient energy losses. Regarding the charging processes in PCM1 (Fig. 11) and PCM2 (Fig. 13), PCM2 undergoes phase change faster than PCM1. As PCM2 has a lower melting temperature than PCM1, the temperature gradient during melting is larger, accelerating the charging process of the layer. Nevertheless, by $t = 24$ h, both PCM layers are fully charged.

4.2.3. Energy output

Fig. 14 shows the transient temperature and mass flow rate profiles of the molten salt streams at the TES outlet and HX inlet during discharge. As the TES discharges, the molten salt outlet temperature gradually decreases from 550 °C to 472 °C, with a nearly isothermal interval around 504 °C. This interval occurs after the molten salt has removed most of the sensible heat from the PCMs' liquid phase and begins to absorb latent heat, as also seen in the temperature and liquid fraction profiles. To maintain a constant thermal power supply of 16 MW to the heat-demanding application, the pump compensates by increasing the molten salt mass flow rate through the TES from 21.1 to 29.5 kg/s. The TES outlet stream mixes with the high-temperature stream from the HRU, increasing the molten salt's temperature and keeping it above 500 °C, thereby meeting the requirements.

Table 8 summarizes the annual energy outputs that serve as the basis for the economic indicators. Each pair of cases is compared according to its corresponding energy output. Specifically, cases AI and AII evaluate the LCOE based on the annual electricity generated through the power block. Alternatively, cases BI and BII assess the LCOH using the annual heat supplied to the heat-demanding application during discharge, including TES and HRU contributions. Finally, cases CI and CII evaluate the LCOS, accounting only for the annual energy stored in the TES.

4.2.4. Economic analysis

Table 9 compares the two-tank molten salt TES and the hybrid PCM–molten salt TES through a breakdown of component costs. The main cost savings come from the storage material, as the PCMs used are more than four times cheaper than solar salt per kilogram. Additionally, the hybrid TES requires less material because of the higher energy storage density of PCMs. Moreover, since the hybrid TES consists of a single multi-layered tank with lower volume and weight, costs related to foundation and sitework are considerably reduced. The main downside of the hybrid design is the internal tube layout, which accounts for more than 25% of its total cost. Overall, the hybrid design reduces the TES capital cost by approximately 28.4% compared to the two-tank molten salt approach.

Table 10 lists the capital and operating cost for each sub-system (in thousand USD).

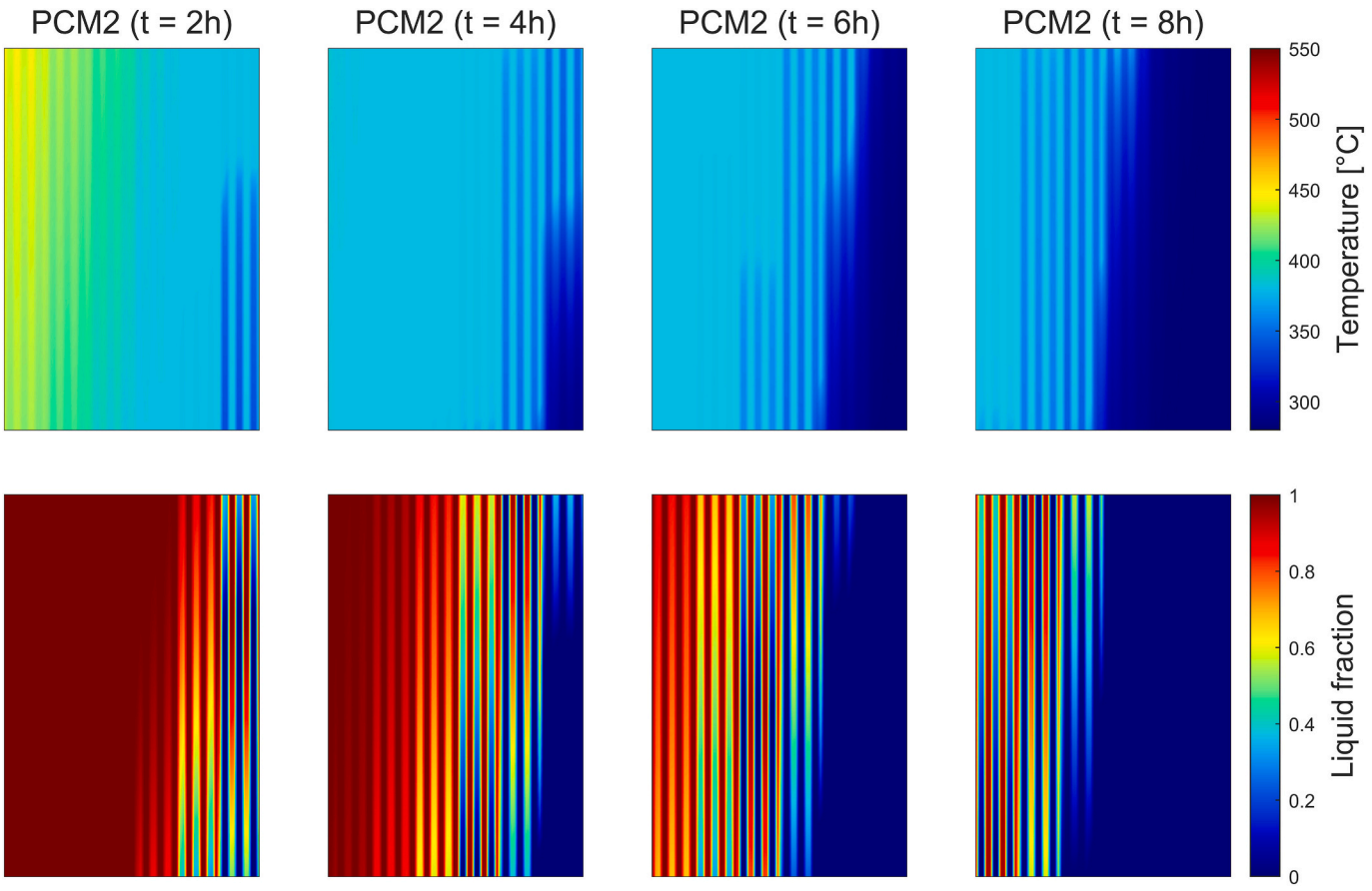

Fig. 12. PCM temperature (top) and liquid fraction (bottom) profiles for PCM layer 2 during discharging.

4.3. Optimization

To further improve the economic performance of the hybrid TES, we conducted a multivariable optimization, using the system cost as the objective function. The optimization considers three decision variables: the energy storage capacity split between PCM layer 1 and PCM layer 2, the tube pitch in PCM layer 1, and the tube pitch in PCM layer 2. As the tube pitch depends on the number of tubes in each layer, these variables take discrete values. The analysis evaluated 31 storage capacity splits between 75%–25% and 45%–55% (PCM1/PCM2). For each one, we tested three tube pitch values in PCM layer 1 and two in PCM layer 2, resulting in 186 cases. We simulated each case in MATLAB to analyze the cycling performance, associated costs, and the molten salt outlet temperature supplied to the heat-demanding application.

Fig. 15 presents the optimization results. In panel (a), we plot the tube pitch in PCM layer 1, and in panel (b), the tube pitch in PCM layer 2, both against the cost reduction relative to the two-tank TES. The color gradient represents the storage capacity split, while the marker shape indicates the molten salt outlet temperature.

The result highlights two trade-offs. The first relates to tube density, which affects the TES performance. A higher density ensures the required outlet temperature but increases the cost. In contrast, lower density significantly reduces costs but fails to meet the temperature requirement. The second trade-off relates to the energy storage distribution between the PCM layers. Increasing the PCM2 storage share reduces costs, since the TES requires fewer internal tubes for charging; however, it lowers the outlet temperature because the TES stores less high-temperature energy. Contrarily, allocating more storage for PCM1 ensures the required outlet temperature but demands a higher internal tube density for charging the TES, raising the cost.

The optimal case was a 67%–33% storage capacity split between PCM1 and PCM2, with tube pitches of 71.8 mm in layer 1 and 74.2 mm in layer 2. The results show that using two PCM layers with different melting temperatures allows the system to meet the design requirements without relying on excessively small tube pitches. The optimization also offers design guidance on appropriate tube pitch and storage capacity split for hybrid TES.

4.4. Economic indicators for the optimized case

Fig. 16 illustrates and lists the levelized costs of electricity, heat, and storage for the two-tank molten salt TES and the hybrid PCM–molten salt TES. The optimized case of the hybrid TES design reduces the LCOE, LCOH, and LCOS by 2.6%, 12.4%, and 33.2%, respectively. The LCOE shows the smallest reduction because the power block cost dominates over the other subsystem costs. In contrast, the LCOH and LCOS exhibit larger reductions, as the TES accounts for a greater share of the capital costs in these cases. These results highlight the economic advantage of the hybrid TES design, particularly for applications that focus on heat supply and storage.

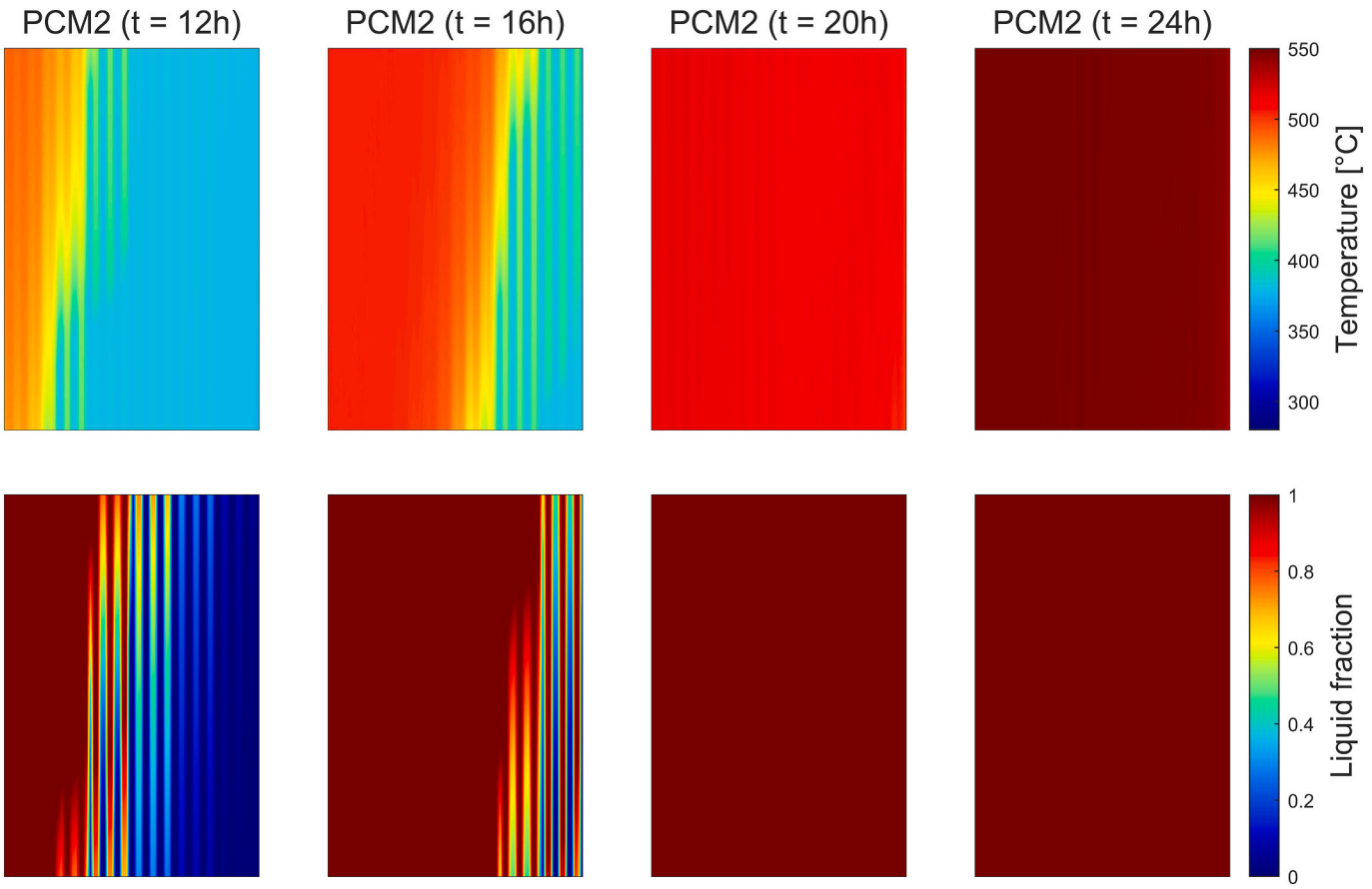

Fig. 13. PCM temperature (top) and liquid fraction (bottom) profiles for PCM layer 2 during charging.

Additionally, the arrangement achieves a considerable cost reduction in both heat and electricity compared to the European benchmark for non-household consumers. In the least favorable case (two-tank TES), the LCOH is nearly four times lower than the natural gas price, reported as 0.0541€/kWh$_{th}$ (0.0632$/kWh$_{th}$) in 2024 [49]. Similarly, the LCOE using the two-tank configuration is about 33% lower than the average electricity price of 0.16€/kWh (0.187$/kWh) in 2024 [50]. These low costs result from utilizing waste heat as the energy source, eliminating fuel expenses. These findings underscore the economic potential of high-grade waste heat recovery in industrial applications.

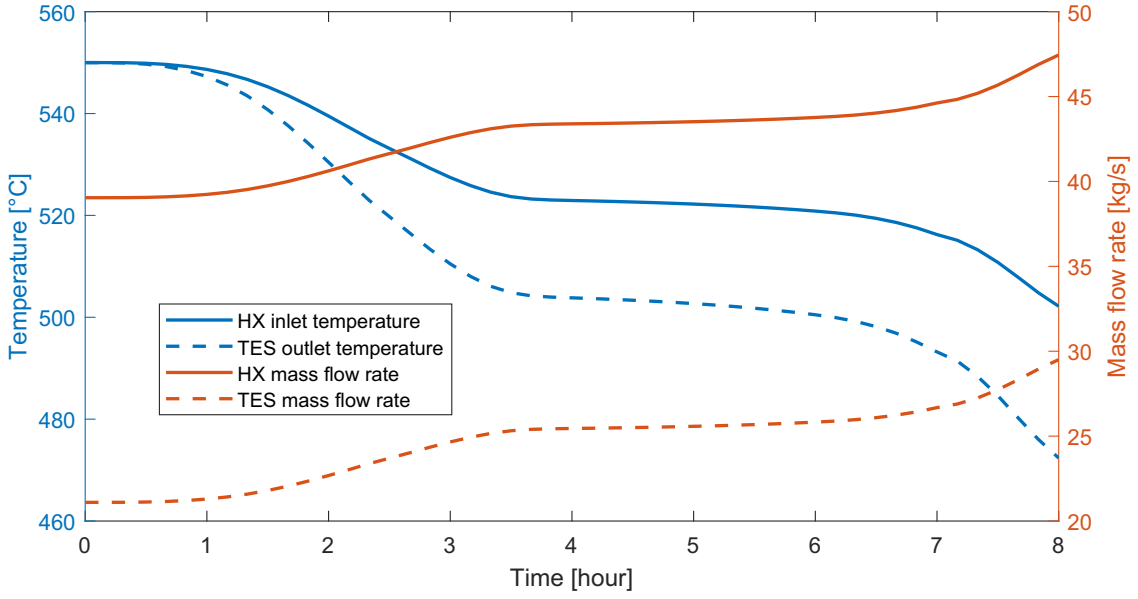

Fig. 14. Variation of temperature and mass flow rate of the molten salt streams at the TES outlet and HX inlet during discharge.

Table 8
Annual energy outputs used for evaluating the economic indicators in each pair of cases.

Cases	Economic indicator	Variable	Units	Case I	Case II
A	LCOE	Electricity generated	MWh_e	15,600	15,367
B	LCOH	Heat supplied	MWh_{th}	38,400	38,400
C	LCOS	Heat stored	MWh_{th}	20,753	20,753

Table 9
Breakdown of component costs for two-tank molten salt TES and hybrid PCM-molten salt TES.

Component	Units	Two-tank TES	Hybrid TES
Molten salt inventory	kUSD	867.47	24.11
PCM 1 inventory	kUSD	–	58.79
PCM 2 inventory	kUSD	–	63.31
Hot tank (stainless steel)	kUSD	375.91	–
Cold tank (carbon steel)	kUSD	158.28	–
External shell (stainless steel)	kUSD	–	339.27
Middle shell (stainless steel)	kUSD	–	171.28
Internal shell (stainless steel)	kUSD	–	12.43
Tank insulation	kUSD	138.49	103.87
Structural steel	kUSD	19.79	9.89
Foundation + Sitework	kUSD	138.49	69.25
Instrumentation and electrical	kUSD	19.79	59.35
Internal tubes (material)	kUSD	–	199.24
Headers, fittings, and tube installation	kUSD	–	119.54
Total	kUSD	1718.21	1230.32

5. Conclusions

This article presented a novel multi-layered hybrid TES concept that combines PCMs and molten salts to achieve high energy storage densities without compromising cycling behavior or heat transfer performance. The design employs two concentric PCM layers with different melting temperatures and a central molten salt core. The external PCM layer enhances charging through its high temperature gradient with the molten salt in the internal tubes, while the internal PCM layer ensures that the molten salt reaches the required outlet temperature. The molten salt in the core serves as the heat transfer fluid and a thermal buffer during mass fluctuations.

The article assessed the feasibility of the hybrid TES for high-temperature waste heat recovery against the two-tank molten salt TES technology. The optimized hybrid configuration reduces the LCOE, LCOH, and LCOS by up to 2.6%, 12.4%, and 33.2% respectively. The standalone TES case shows the greatest improvement since it accounts for the full capital cost of the system. Moreover, the waste heat recovery strategy with both TES configurations demonstrates clear economic competitiveness compared to the European benchmark for non-household consumers. The heat recovery is four times less expensive than burning natural gas, while the generated electricity is about 33% cheaper than the average European price in 2024.

The optimization revealed two main trade-offs. The first trade-off involves the internal tube density, where a higher density improves TES thermal performance by raising the outlet molten salt temperature but also increases system costs. The second trade-off concerns the allocation of energy storage capacity between the PCM layers. A larger share of PCM2 (low melting temperature) enhances the TES heat transfer rate because of the higher temperature gradient with the molten salt, requiring fewer internal tubes for charging; however, it lowers the maximum outlet temperature since less high-temperature energy is stored. In contrast, a larger share of PCM1 (high melting temperature) increases the storage of high-temperature energy, but it requires higher tube density to achieve effective charging cycles.

The study employed PCM thermophysical properties reported in the literature, with pricing estimated from pure constituent substances. Since the design relies on literature-based properties, further advances in commercially available high-temperature PCMs are important to support the practical implementation of this concept. Future work will investigate the integration of the hybrid TES into systems where storage plays a more significant role, such as CSP plants and Carnot batteries for electricity arbitrage.

CRediT authorship contribution statement

Daniel Aviles: Writing – original draft, Visualization, Software, Methodology, Investigation, Formal analysis, Conceptualization. **Emanuele Zanetti:** Writing – review & editing, Supervision, Conceptualization. **Simone Mancin:** Writing – review & editing, Conceptualization. **Kamel Hooman:** Writing – review & editing, Supervision, Project administration, Conceptualization.

Declaration of competing interest

The authors declare that they have no known competing financial interests or personal relationships that could have appeared to influence the work reported in this paper.

Table 10
Capital and operating costs for each sub-system.

Sub-system	Units	A I	A II	B I	B II	C I	C II
Power block–capital cost*	kUSD	12,025	12,025	–	–	–	–
Power block–operating cost	kUSD/y	484	483	–	–	–	–
HX–capital cost*	kUSD	–	–	1177	1177	–	–
HX–operating cost	kUSD/y	–	–	55	55	–	–
HRU–capital cost*	kUSD	1926	1926	1926	1926	–	–
HRU–operating cost	kUSD/y	90	90	90	90	–	–
TES–capital cost*	kUSD	1838	1316	1838	1316	1838	1316
TES–operating cost	kUSD/y	85.9	61.5	85.9	61.5	85.9	61.5

* Capital costs include a 7% contingency.

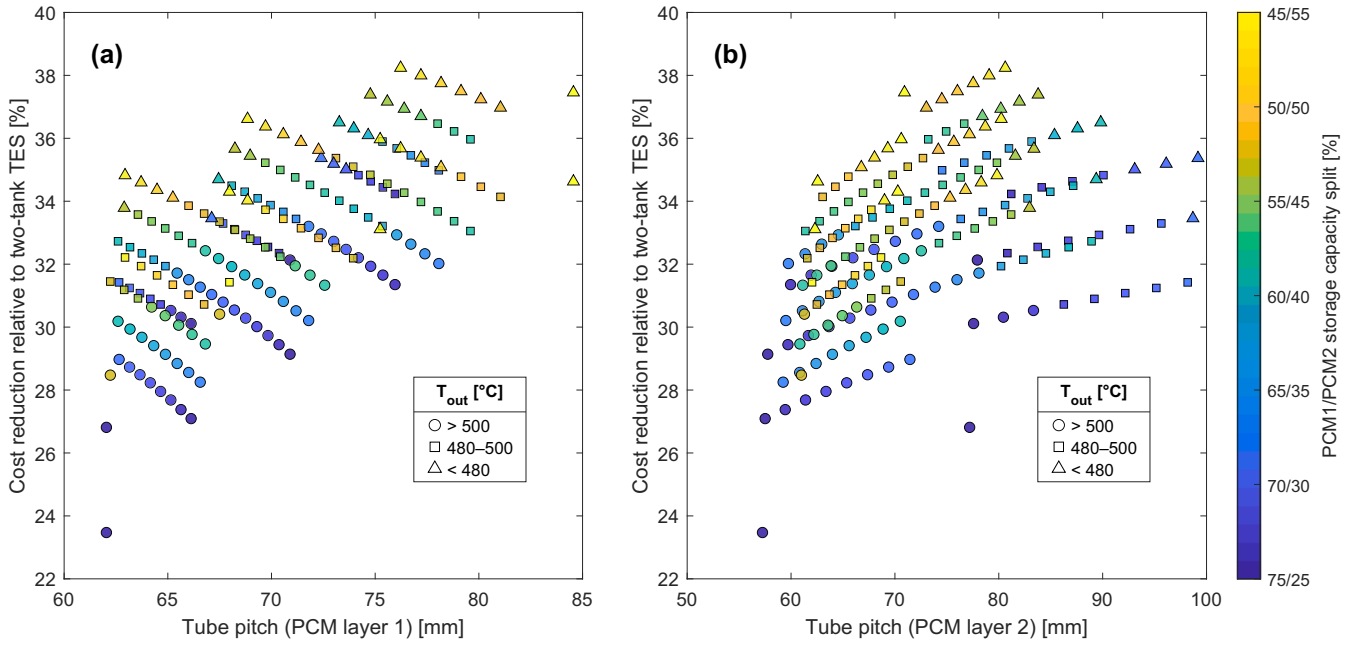

Fig. 15. Cost reduction of the hybrid TES relative to a two-tank TES as a function of tube pitch in (a) PCM layer 1 and (b) PCM layer 2. Color indicates the storage capacity split, and marker shape indicates the outlet temperature.

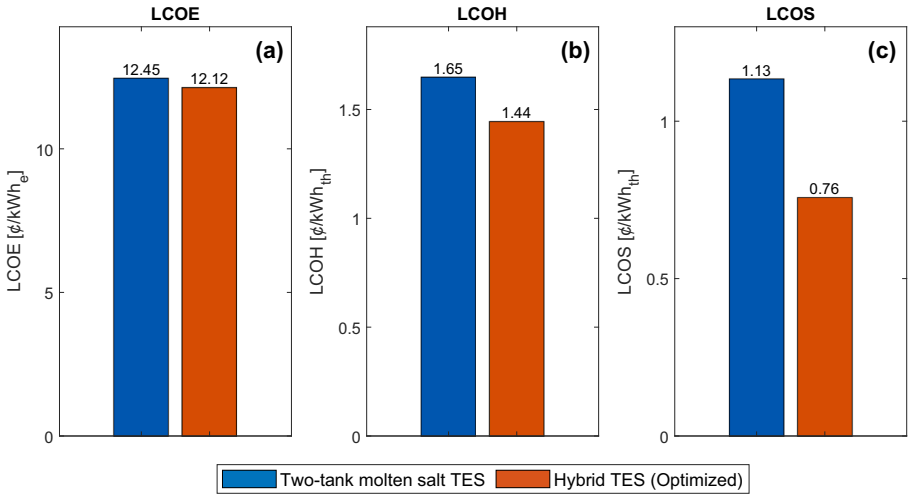

Fig. 16. Comparison of levelized costs between the two-tank and hybrid TES: (a) LCOE, (b) LCOH, and (c) LCOS.

Data availability

Data will be made available on request.

Appendix A. Estimated prices of pure constituent substances

Table A.1 lists indicative prices for the pure constituent substances. These values were compiled from multiple suppliers and specialized commodity-market reports [51], covering different regions over the period 2023–2025. Reported prices are approximations, as they vary depending on the demand and the region.

Table A.1
Estimated prices of pure constituent substances.

Pure constituent	Unit	Value
$MgCl_2$	$/MT	275
KCl	$/MT	370

(*continued on next page*)

Table A.1 (*continued*)

Pure constituent	Unit	Value
NaCl	$/MT	78
Li_2CO_3	$/MT	11,100
$CaCl_2$	$/MT	230
$BaCl_2$	$/MT	450
Na_2CO_3	$/MT	270
K_2CO_3	$/MT	1000

Appendix B. Influence of flow arrangement on the TES outlet temperature

This appendix illustrates the effect of the flow arrangement on the TES outlet temperature and provides additional support for the selection of Configuration 3. Fig. B.1 shows the TES outlet temperature during discharge for configurations with a similar total number of tubes per layer but different numbers of rows per header.

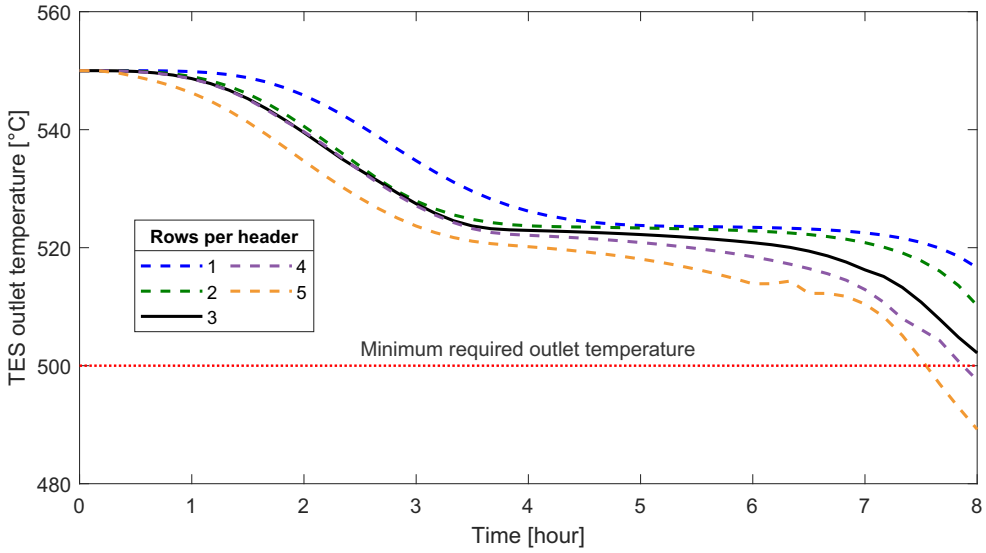

Fig. B.1. TES outlet temperature during discharge for configurations with a similar total number of tubes but different numbers of rows per header.

As the number of rows per header increases, the TES outlet temperature decreases more rapidly over time, as the molten salt circulates fewer times over each layer, ultimately failing to meet the target outlet temperature of 500 °C. In contrast, reducing the number of rows per header results in higher outlet temperatures over time, but it also increases system complexity and pumping requirements. Considering the trade-off between the TES outlet temperature and system complexity, we selected three rows of tubes per header for this study.

References

[1] European Commission, Stepping up Europe's 2030 Climate Ambition - Investing in a Climate-Neutral Future for the Benefit of our People (COM(2020) 562 Final), Brussels, Sep. 2020.
[2] E. C. D.-G. for C. Action, Going Climate-Neutral by 2050 – A Strategic Long-Term Vision for a Prosperous, Modern, Competitive and Climate-Neutral EU Economy, Publications Office, 2019, https://doi.org/10.2834/02074.
[3] IEA, World Energy Outlook 2024, Paris. [Online]. Available: https://www.iea.org/reports/world-energy-outlook-2024, 2024.
[4] K.M. Adamson, et al., High-temperature and transcritical heat pump cycles and advancements: a review, Renew. Sustain. Energy Rev. 167 (Oct. 2022) 112798, https://doi.org/10.1016/J.RSER.2022.112798.
[5] H. Jouhara, A.G. Olabi, Editorial: industrial waste heat recovery, Energy 160 (Oct. 2018) 1–2, https://doi.org/10.1016/J.ENERGY.2018.07.013.
[6] C.A. Schoeneberger, C.A. McMillan, P. Kurup, S. Akar, R. Margolis, E. Masanet, Solar for industrial process heat: a review of technologies, analysis approaches, and potential applications in the United States, Energy 206 (Sep. 2020) 118083, https://doi.org/10.1016/J.ENERGY.2020.118083.
[7] M. Ja'fari, M.I. Khan, S.G. Al-Ghamdi, A.J. Jaworski, F. Asfand, Waste heat recovery in iron and steel industry using organic Rankine cycles, Chem. Eng. J. 477 (Dec. 2023) 146925, https://doi.org/10.1016/J.CEJ.2023.146925.
[8] E. Delikonstantis, M. Camerin, L. Chion, S.A. Theofanidis, E. Benetto, A. Bertrand, Waste heat recovery and valorization to electricity and steam: use of Heat2Power® tool in a real case study from the steel industry, Chem. Eng. Process. Process Intensif. 203 (Sep. 2024) 109896, https://doi.org/10.1016/J.CEP.2024.109896.
[9] W. Sun, Q. Wang, Y. Zhou, J. Wu, Material and energy flows of the iron and steel industry: status quo, challenges and perspectives, Appl. Energy 268 (Jun. 2020) 114946, https://doi.org/10.1016/J.APENERGY.2020.114946.
[10] M. Papapetrou, G. Kosmadakis, A. Cipollina, U. La Commare, G. Micale, Industrial waste heat: estimation of the technically available resource in the EU per industrial sector, temperature level and country, Appl. Therm. Eng. 138 (Jun. 2018) 207–216, https://doi.org/10.1016/J.APPLTHERMALENG.2018.04.043.
[11] M.T. Holzleitner-Senck, S. Moser, M. Denk, Waste heat inconsistencies in the EU's energy legislation, Util. Policy 93 (Apr. 2025) 101880, https://doi.org/10.1016/J.JUP.2024.101880.
[12] G. Manente, Y. Ding, A. Sciacovelli, A structured procedure for the selection of thermal energy storage options for utilization and conversion of industrial waste heat, J. Energy Storage 51 (Jul. 2022) 104411, https://doi.org/10.1016/J.EST.2022.104411.
[13] I. Alshehhi, W. Alnahdi, M.I. Hassan Ali, A. Bouabid, A. Sleptchenko, Assessment of waste heat recovery in the steel industry, J. Sustain. Dev. Energy Water Environ. Syst. 11 (2) (Jun. 2023), https://doi.org/10.13044/J.SDEWES.D10.0440.
[14] I. Ortega-Fernández, J. Rodríguez-Aseguinolaza, Thermal energy storage for waste heat recovery in the steelworks: the case study of the REslag project, Appl. Energy 237 (Mar. 2019) 708–719, https://doi.org/10.1016/J.APENERGY.2019.01.007.
[15] I. Wolde, J.M. Cardemil, R. Escobar, Compatibility assessment of thermal energy storage integration into industrial heat supply and recovery systems, J. Clean. Prod. 440 (Feb. 2024) 140932, https://doi.org/10.1016/J.JCLEPRO.2024.140932.
[16] M. Mehos, C. Turchi, J. Jorgenson, P. Denholm, C. Ho, K. Armijo, On the Path to SunShot - Advancing Concentrating Solar Power Technology, Performance, and Dispatchability, United States, 2016, https://doi.org/10.2172/1344199.

[17] D. Aviles, F. Sabri, K. Hooman, Techno-economic analysis of a hybrid solar-geothermal power plant integrated with a desalination system, Int. J. Energy Res. 45 (12) (Oct. 2021) 17955–17970, https://doi.org/10.1002/ER.6948.
[18] S. Tiari, A. Hockins, M. Mahdavi, Numerical study of a latent heat thermal energy storage system enhanced by varying fin configurations, Case Stud. Therm. Eng. 25 (Jun. 2021) 100999, https://doi.org/10.1016/J.CSITE.2021.100999.
[19] C. Prieto, L.F. Cabeza, Thermal energy storage (TES) with phase change materials (PCM) in solar power plants (CSP). Concept and plant performance, Appl. Energy 254 (Nov. 2019) 113646, https://doi.org/10.1016/J.APENERGY.2019.113646.
[20] C. Zhou, S. Wu, Medium- and high-temperature latent heat thermal energy storage: material database, system review, and corrosivity assessment, Int. J. Energy Res. 43 (2) (Feb. 2019) 621–661, https://doi.org/10.1002/ER.4216.
[21] J.C. Gomez, High-Temperature Phase Change Materials (PCM) Candidates for Thermal Energy Storage (TES) Applications, 2011, https://doi.org/10.2172/1024524.
[22] C. Prieto, L.F. Cabeza, Thermal energy storage with phase change materials in solar power plants. Economic analysis, J. Energy Storage 43 (Nov. 2021) 103184, https://doi.org/10.1016/J.EST.2021.103184.
[23] G. Alva, L. Liu, X. Huang, G. Fang, Thermal energy storage materials and systems for solar energy applications, Renew. Sustain. Energy Rev. 68 (Feb. 2017) 693–706, https://doi.org/10.1016/J.RSER.2016.10.021.
[24] B. Nie, A. Palacios, B. Zou, J. Liu, T. Zhang, Y. Li, Review on phase change materials for cold thermal energy storage applications, Renew. Sustain. Energy Rev. 134 (Dec. 2020) 110340, https://doi.org/10.1016/J.RSER.2020.110340.
[25] B. Sun, Z. Liu, X. Ji, L. Gao, D. Che, Thermal energy storage characteristics of packed bed encapsulating spherical capsules with composite phase change materials, Appl. Therm. Eng. 201 (Jan. 2022) 117659, https://doi.org/10.1016/J.APPLTHERMALENG.2021.117659.
[26] S.S. Mostafavi Tehrani, Y. Shoraka, K. Nithyanandam, R.A. Taylor, Cyclic performance of cascaded and multi-layered solid-PCM shell-and-tube thermal energy storage systems: a case study of the 19.9 MWe Gemasolar CSP plant, Appl. Energy 228 (Oct. 2018) 240–253, https://doi.org/10.1016/J.APENERGY.2018.06.084.
[27] J. Li, et al., An experimental and numerical study on the energy storage and release performance of shell and tube heat exchangers with phase change material for the data center, Appl. Therm. Eng. 255 (Oct. 2024) 123966, https://doi.org/10.1016/J.APPLTHERMALENG.2024.123966.
[28] A. Fragnito, N. Bianco, M. Iasiello, G.M. Mauro, L. Mongibello, Experimental and numerical analysis of a phase change material-based shell-and-tube heat exchanger for cold thermal energy storage, J. Energy Storage 56 (Dec. 2022) 105975, https://doi.org/10.1016/J.EST.2022.105975.
[29] N. Bianco, A. Fragnito, M. Iasiello, G.M. Mauro, L. Mongibello, Multi-objective optimization of a phase change material-based shell-and-tube heat exchanger for cold thermal energy storage: experiments and numerical modeling, Appl. Therm. Eng. 215 (Oct. 2022) 119047, https://doi.org/10.1016/J.APPLTHERMALENG.2022.119047.
[30] L. Huang, U. Piontek, L. Zhuang, R. Zheng, D. Zou, Retrofitting of a solar cooling and heating plant by employing PCM storage and adjusting control strategy, Appl. Energy 368 (Aug. 2024), https://doi.org/10.1016/j.apenergy.2024.123462.
[31] J. Wang, Y. Ouyang, G. Chen, Experimental study on charging processes of a cylindrical heat storage capsule employing multiple-phase-change materials, Int. J. Energy Res. 25 (5) (Apr. 2001) 439–447, https://doi.org/10.1002/ER.695.
[32] M.M. Farid, A. Kanzawa, Thermal performance of a heat storage module using PCM's with different melting temperatures: mathematical modeling, J. Sol. Energy Eng. 111 (2) (May 1989) 152–157, https://doi.org/10.1115/1.3268301.
[33] H. Shabgard, C.W. Robak, T.L. Bergman, A. Faghri, Heat transfer and exergy analysis of cascaded latent heat storage with gravity-assisted heat pipes for concentrating solar power applications, Solar Energy 86 (3) (Mar. 2012) 816–830, https://doi.org/10.1016/J.SOLENER.2011.12.008.
[34] S.S. Mostafavi Tehrani, R.A. Taylor, K. Nithyanandam, A. Shafiei Ghazani, Annual comparative performance and cost analysis of high temperature, sensible thermal energy storage systems integrated with a concentrated solar power plant, Sol. Energy 153 (Sep. 2017) 153–172, https://doi.org/10.1016/J.SOLENER.2017.05.044.
[35] S.S.M. Tehrani, R.A. Taylor, P. Saberi, G. Diarce, Design and feasibility of high temperature shell and tube latent heat thermal energy storage system for solar thermal power plants, Renew. Energy 96 (Oct. 2016) 120–136, https://doi.org/10.1016/J.RENENE.2016.04.036.
[36] Y.-C. Liu, L.-S. Chao, Modified effective specific heat method of solidification problems, Mater. Trans. 47 (11) (2006) 2737–2744, https://doi.org/10.2320/matertrans.47.2737.
[37] V. Gnielinski, Neue Gleichungen für den Wärme- und den Stoffübergang in turbulent durchströmten Rohren und Kanälen, Forschung im Ingenieurwesen A 41 (1) (1975) 8–16, https://doi.org/10.1007/BF02559682.
[38] F.P. Incropera, D.P. Dewitt, T.L. Bergman, A.S. Lavine, Fundamentals of Heat and Mass Transfer, John Wiley & Sons Inc., Hoboken, NJ., 2002, 981p.
[39] Thermal Conductivity of Stainless Steel Explained & Chart - SteelPRO Group, 2024. Accessed: Aug. 03, 2025. [Online]. Available: https://steelprogroup.com/stainless-steel/properties/thermal-conductivity/.
[40] The MathWorks Inc, MATLAB, The MathWorks Inc., Natick, MA, USA, 2024.
[41] M. Wagner, Simulation and predictive performance modeling of utility-scale central receiver system power plants, Accessed: Aug. 04, 2025. [Online]. Available: https://minds.wisconsin.edu/handle/1793/45001, 2008.
[42] F.R. Martínez, E. Borri, S. Ushak, S. Mani Kala, C. Prieto, L.F. Cabeza, Experimental characterization of phase change materials for thermal energy storage in the temperature range between 270°C and 400°C, Energy 314 (Jan. 2025) 134243, https://doi.org/10.1016/J.ENERGY.2024.134243.
[43] L.F. Cabeza, F.R. Martínez, E. Borri, S. Ushak, C. Prieto, Thermal energy storage using phase change materials in high-temperature industrial applications: multi-criteria selection of the adequate material, Materials 17 (8) (Apr. 2024) 1878, https://doi.org/10.3390/MA17081878.
[44] M. Mehos, et al., Concentrating Solar Power Gen3 Demonstration Roadmap, United States, 2016, https://doi.org/10.2172/1338899.
[45] W. Short, D.J. Packey, T. Holt, A Manual for the Economic Evaluation of Energy Efficiency and Renewable Energy Technologies, National Renewable Energy Lab. (NREL), Golden, CO (United States), 1995.
[46] D. Feldman, M. Bolinger, P. Schwabe, Current and Future Costs of Renewable Energy Project Finance Across Technologies, United States, 2020, https://doi.org/10.2172/1660124.
[47] M.M. Kenisarin, High-temperature phase change materials for thermal energy storage, Renew. Sustain. Energy Rev. 14 (3) (Apr. 2010) 955–970, https://doi.org/10.1016/J.RSER.2009.11.011.
[48] AspenTech, Aspen Exchanger Design and Rating (EDR), *Aspen Technology, Inc.*, 2020. V12.
[49] Eurostat, Gas Prices for Non-household Consumers (nrg_pc_203), 2025, https://doi.org/10.2908/nrg_pc_203.
[50] Eurostat, Electricity Prices for Non-household Consumers (nrg_pc_205), 2025, https://doi.org/10.2908/nrg_pc_205.
[51] Market research company, reports and consulting services | IMARC, 2025. Accessed: Aug. 31, 2025. [Online]. Available: https://www.imarcgroup.com/.